

Evolutionary dynamics of glucose-deprived cancer cells: insights from experimentally-informed mathematical modelling

Luis Almeida ^{*} Jérôme Denis ^{†‡} Nathalie Ferrand [†] Tommaso Lorenzi [§]
 Michèle Sabbah [†] Chiara Villa ^{*}

June 12, 2025

Abstract

Glucose is a primary energy source for cancer cells. Several lines of evidence support the idea that monocarboxylate transporters, such as MCT1, elicit metabolic reprogramming of cancer cells in glucose-poor environments, allowing them to reuse lactate, a byproduct of glucose metabolism, as an alternative energy source with serious consequences for disease progression. We employ a synergistic experimental and mathematical modelling approach to explore the evolutionary processes at the root of cancer cell adaptation to glucose deprivation, with particular focus on the mechanisms underlying the increase in MCT1 expression observed in glucose-deprived aggressive cancer cells. Data from *in vitro* experiments on breast cancer cells are used to inform and calibrate a mathematical model that comprises a partial integro-differential equation for the dynamics of a population of cancer cells structured by the level of MCT1 expression. Analytical and numerical results of this model indicate that environment-induced changes in MCT1 expression mediated by lactate-associated signalling pathways enable a prompt adaptive response of glucose-deprived cancer cells, whilst spontaneous changes due to non-genetic instability create the substrate for environmental selection to act upon, speeding up the selective sweep underlying cancer cell adaptation to glucose deprivation, and may constitute a long-term bet-hedging mechanism.

1 Introduction

Glucose is one of the primary nutrients used by cancer cells to produce energy, and glucose deficiency causes metabolic stress, cell dysfunction, and eventual death [1]. In fact, glucose consumption not only results in decreased nutrient availability, but also generally correlates with lactate production and the development of an acidic extracellular environment [2–4]. Cancer cells can rely on a variety of mechanisms that activate protective functions under metabolic and environmental stress, including metabolic reprogramming [5]. Accumulating evidence indicates that aggressive cancer cells may acquire the ability to absorb lactic acid and use it to synthesise pyruvate [3, 6, 7], thus converting harmful byproducts of glucose metabolism into alternative energy sources. Lactic acid is transported across cell membranes through a family of four reversible monocarboxylate transporters (MCTs) belonging to the SLC16/MCT family of solute carriers [8]. Amongst these, MCT1 is the most widely expressed and facilitates lactate and pyruvate upload [9, 10]. Such an increase in pyruvate and lactate metabolism has been associated with enhanced invasion and migration, and higher survival in the circulation, with overall consequences

^{*}Sorbonne Université, CNRS, Université de Paris, Inria, Laboratoire Jacques-Louis Lions UMR 7598, 75005 Paris, France

[†]Sorbonne Université, Cancer Biology and Therapeutics, INSERM, CNRS, Institut Universitaire de Cancérologie, Saint-Antoine Research Center (CRSA), F-75012, Paris, France

[‡]Department of Endocrinology and Oncology Biochemistry, Pitié-Salpêtrière Hospital, 75013 Paris, France

[§]Department of Mathematical Sciences “G. L. Lagrange”, Dipartimento di Eccellenza 2018-2022, Politecnico di Torino, 10129 Torino, Italy

for metastasis [11,12], to the extent that MCT1 inhibition has been investigated as a potential therapeutic target [13,14].

While it is evident that the overexpression of MCT1 plays a key role in the metabolic reprogramming of glucose-deprived aggressive cancer cells, allowing them to reuse lactate as an alternative energy source with serious consequences for disease progression, the mechanisms underlying such a change in MCT1 expression remain, to this day, poorly explored. On the one hand, lactate may function as a signalling molecule, triggering regulatory pathways that modify the transcriptional activity of MCT1 [6,15], thus mediating environment-induced changes in MCT1 expression [16]. On the other hand, cancer cells are known to undergo spontaneous heritable and reversible changes in gene expression due to non-genetic instability [17,18]. This is generally associated with noise in gene expression and may be due, for instance, to DNA methylation or histone modifications [19,20] occurring over the lifespan of a tumour cell. As lactate has been shown to be responsible for certain histone modifications [21,22], the effect of non-genetic instability may even be enhanced under glucose-deprivation.

In this work, a synergistic experimental and mathematical modelling approach is employed to explore the evolutionary processes at the root of cancer cell adaptation to glucose deprivation, with particular focus on the mechanisms underlying the increase in MCT1 expression observed in glucose-deprived aggressive cancer cells. Data from *in vitro* experiments on breast cancer cells, which were specifically carried out for this study, are used to inform a mathematical model that comprises a partial integro-differential equation (PIDE) for the dynamics of a population of cancer cells structured by the level of MCT1 expression, which is coupled with a system of ordinary differential equations (ODEs) for the dynamics of glucose and lactate present in the extracellular environment. This model allows for predictions on the dynamics of the MCT1 expression distribution of cancer cells to be made and to be directly compared with the results of flow cytometry analyses, while making it also possible to dissect out the evolutionary processes underlying these dynamics. Related mathematical models have been employed to investigate cancer cell adaptation to hypoxia [23–30], but not to assess MCT1-associated changes in lactate uptake. Furthermore, alternative mathematical models have been proposed to study the role of MCT1 expression-regulated lactate uptake in the coexistence of different metabolic pathways within the same tumour [4,31,32], but none of these proposes a causal mechanism for the reported increase in MCT1 expression.

Experimental data are used to carry out model calibration, through a likelihood-maximising method [33–35], and the results of numerical simulations of the calibrated model are complemented with analytical results on the qualitative and quantitative properties of the solution to the PIDE that governs the evolution of cancer cells. These results shed light on the evolutionary dynamics of glucose-deprived cancer cells by elucidating the respective roles that environment-induced changes in MCT1 expression mediated by lactate-associated signalling pathways and spontaneous changes due to non-genetic instability play in the adaptation of cancer cell populations to glucose-poor environments.

2 Methods

2.1 *In vitro* experiments

A summary of the experimental set-up is provided below, and full details of experimental materials and methods can be found in Sup.Mat.S2.

Cell lines

Breast cancer cells of the MCF7 and MCF7-sh-WISP2 lines are considered, with the latter being obtained from the former upon inducing epithelial-to-mesenchymal transition through WISP2 gene silencing. The focus of this study is on the MCF7-sh-WISP2 cell line, which has been documented to be more invasive and aggressive than the MCF7 cell line [36,37]. We also report on the results from experiments conducted on MCF7 cells to corroborate the hypothesis that fast metabolic reprogramming associated with lactate uptake under glucose deprivation is characteristic of more aggressive cancer cells.

‘Glucose-deprivation’ and ‘rescue’ experiments

Cells originally maintained in medium containing 4.5g/l of glucose (i.e. a high level of glucose) are seeded, at high cell numbers, in a medium containing 1g/l of glucose (i.e. a physiological level of glucose). In ‘glucose-deprivation’ experiments, glucose is not re-added to the medium during cell culture (i.e. there is no glucose replenishment) so that, due to consumption by the cells, glucose levels drop during the course of the experiment and thus cells experience glucose deprivation. In ‘rescue’ experiments, a similar protocol is followed for a few days and the culture medium is subsequently changed to a medium containing 4.5g/l of glucose, where cells are cultured for a few more days, so that cells first experience glucose deprivation and are then rescued from it.

Measured quantities

Over the span of several days, we tracked: viable cell numbers and percentages of apoptotic cells; glucose and lactate concentrations in the cell culture medium; MCT1 expression distribution (i.e. fluorescence-intensity distributions), obtained through flow cytometry analysis and complemented with images from immunocytochemistry analysis; mRNA expression of different MCT proteins measured by RT-qPCR – i.e. MCT1, MCT2 (an MCT very similar to MCT1 although it displays a higher affinity for L-lactic acid and pyruvate), and MCT4 (an efficient lactate exporter expressed in glycolytic cells that is not required for lactate uptake [9, 10]).

2.2 Mathematical modelling

Building on the modelling strategies presented in [38,39], we develop a mathematical model that describes the evolutionary dynamics of a population of MCF7-sh-WISP2 cells, structured by the level of MCT1 expression, under the environmental conditions which are determined by the levels of glucose and lactate in the extracellular environment. An outline of the model is provided below, while a detailed description of the model equations alongside the main modelling assumptions, which are informed by the results of *in vitro* experiments underlying this study, is provided in Sup.Mat.S1.

Key model quantities

The model comprises a PIDE for the dynamics of the cell population density function $n(t, y)$, which represents the number of MCF7-sh-WISP2 cells with level of MCT1 expression $y \in \mathbb{R}$ at time $t \in \mathbb{R}_+$ (i.e. the MCT1 expression distribution of MCF7-sh-WISP2 cells at time t). Such a PIDE is coupled with a system of ODEs for the dynamics of the concentrations of glucose and lactate in the extracellular environment $G(t)$ and $L(t)$. The cell number, the mean level of MCT1 expression and the related variance, which provides a possible measure for the level of intercellular variability in MCT1 expression, are computed, respectively, as

$$\rho(t) = \int_{\mathbb{R}} n(t, y) dy, \quad \mu(t) = \frac{1}{\rho(t)} \int_{\mathbb{R}} y n(t, y) dy, \quad \sigma^2(t) = \frac{1}{\rho(t)} \int_{\mathbb{R}} y^2 n(t, y) dy - \mu^2(t). \quad (2.1)$$

Modelling cell proliferation and death under environmental selection on MCT1 expression

The results of *in vitro* experiments (cf. Sec. 3.2) indicate that the MCT1 expression distribution of MCF7-sh-WISP2 cells is, to a first approximation, unimodal with a single peak at the centre of the distribution. The location of the centre of the distribution moves from lower to higher expression levels when cells experience glucose deprivation and from higher to lower expression levels when cells are rescued from glucose deprivation. Hence, we assume that there is a level of MCT1 expression (i.e. the fittest level of MCT1 expression) endowing cells with the highest fitness depending on the environmental conditions determined by the concentrations of glucose and lactate. Moreover, the results of *in vitro* experiments (cf. Sec. 3.1) support the idea that proliferation and survival of MCF7-sh-WISP2 cells correlate with glucose uptake when glucose levels are sufficiently high and with lactate uptake when glucose levels are

low. Therefore, we further assume that there are a level of MCT1 expression, y_L , endowing cells with the highest rate of proliferation via glycolysis and a higher level of MCT1 expression, $y_H > y_L$, endowing cells with the highest rate of proliferation via lactate reuse when glucose is scarce – i.e. if the concentration of glucose in the extracellular environment is lower than a threshold level G^* above which cells stop taking lactate from the extracellular environment in order to prioritise glucose uptake. Under these assumptions, in the framework of our model, the fittest level of MCT1 expression is represented by the function $Y(G, L)$, defined via Eq. (S.14) in Sup.Mat.S1, which is such that if $G \geq G^*$ then $Y(G, L) = y_L$ for any $L \geq 0$, whereas if $G < G^*$ then $Y(G, L) \rightarrow y_H$ as G decreases and L increases. Furthermore, the strength of environmental selection on MCT1 expression is linked to the value of the selection gradient $b(G, L)$ defined via Eq. (S.12) in Sup.Mat.S1,

Modelling spontaneous and environment-induced changes in MCT1 expression

The effects of changes in the level of cell expression of MCT1 are also incorporated into the model. In particular, we let spontaneous changes due to non-genetic instability occur at rate Φ . Moreover, we assume that environment-induced changes mediated by lactate-associated signalling pathways lead to an increase in MCT1 expression at rate Ψ^+ under glucose deprivation (i.e. when $G < G^*$) and to a decrease in MCT1 expression at rate Ψ^- when the glucose level is sufficiently high (i.e. when $G \geq G^*$).

2.3 Model calibration based on experimental data

Experimental data on MCF7-sh-WISP2 cells are used to carry out model calibration through a likelihood-maximising method [33–35]. In summary, the mathematical model and the data are first nondimensionalised to avoid calibration bias. Then the optimal parameter set (OPS) is obtained, through an iterative process, by maximising the likelihood, defined assuming Gaussian measurement noise with zero mean, exploiting the in-built MATLAB function `bayesopt`, which is based on Bayesian Optimisation. At each iteration, we solve numerically the PIDE-ODE system that constitutes the model, using the methods described in Sup.Mat.S2. The MATLAB source code along with the data used for model calibration have been made available on GitHub¹. In order to explore a variety of evolutionary scenarios, calibration was carried out for the model in which both spontaneous and environment-induced changes in MCT1 expression are included (i.e. $\Phi \not\equiv 0$ and $\Psi^\pm \not\equiv 0$), and for reduced models that take into account only spontaneous (i.e. $\Phi \not\equiv 0$ and $\Psi^\pm \equiv 0$) or environment-induced (i.e. $\Phi \equiv 0$ and $\Psi^\pm \not\equiv 0$) changes. The obtained OPSs are reported in Tab.S1 in Sup.Mat.S2.

2.4 Simulation and analysis of the model

To explore the mechanisms underlying the evolutionary dynamics of MCF7-sh-WISP2 cells under glucose deprivation, the results of numerical simulations of the calibrated model, which are carried out using the numerical methods described in Sup.Mat.S2.4, are integrated with the analytical results presented in Sup.Mat.S2.5, which build on the results presented in [30, 40–43].

3 Main results

3.1 Proliferation and survival of MCF7-sh-WISP2 cells correlate with lactate uptake under glucose deprivation

Fig.1 and Fig.S1 in Sup.Mat.S3 summarise the dynamics of cell proliferation and glucose and lactate concentrations in the cell culture medium observed during ‘glucose-deprivation’ experiments conducted for four days on MCF7-sh-WISP2 and MCF7 cells, respectively. The corresponding dynamics of cell death are summarised by Fig.S2 in Sup.Mat.S3. These results demonstrate that there is a stark difference in the proliferation dynamics of the MCF7-sh-WISP2 and MCF7 cell lines under glucose deprivation, with

¹<https://github.com/ChiaraVilla/AlmeidaEtAl2023Evolutionary>

the former reaching numbers of viable cells over twice as high as the latter. Moreover, cell death in the MCF7-sh-WISP2 line does not significantly increase over time, as opposed to the MCF7 line for which the percentage of apoptotic cells undergoes a four-fold increase during the experiment. The dynamics of the concentration of glucose in the culture medium of the two cell lines are similar, though only cells of the MCF7-sh-WISP2 line consume all the glucose available. Furthermore, the concentration of lactate in the culture medium of MCF7 cells displays a steady increase mirroring glucose consumption, whilst a decline in lactate concentration in the culture medium of MCF7-sh-WISP2 cells is observed when little to no glucose is present in the medium, thus suggesting that lactate uptake occurs amongst MCF7-sh-WISP2 cells under glucose deprivation. Taken together, these experimental results support the idea that proliferation and survival of MCF7-sh-WISP2 cells correlate with glucose consumption when glucose levels are sufficiently high and with lactate uptake under glucose deprivation.

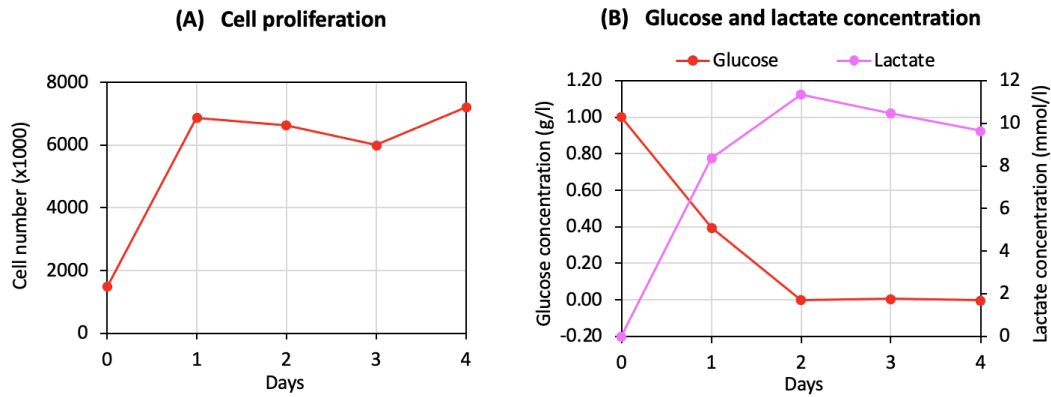


Figure 1: **Dynamics of cell proliferation and glucose and lactate concentrations in ‘glucose-deprivation’ experiments conducted on MCF7-sh-WISP2 cells.** Dynamics of cell proliferation (panel (A)), glucose concentration (panel (B), red line, left y-axis) and lactate concentration (panel (B), pink line, right y-axis) in ‘glucose-deprivation’ experiments conducted on MCF7-sh-WISP2 cells for four days. Cell proliferation was assessed by counting the number of viable cells upon seeding (i.e. day 0) and at the end of each day of culture (i.e. days 1-4). Glucose and lactate concentrations were measured in the cell culture medium on days 0-4.

3.2 Glucose deprivation induces a reversible increase in MCT1 expression of MCF7-sh-WISP2 cells

The experimental results summarised by Fig.2 show a steady increase in MCT1 expression of MCF7-sh-WISP2 cells throughout ‘glucose-deprivation’ experiments. On the other hand, in ‘rescue’ experiments, MCT1 expression levels of MCF7-sh-WISP2 cells increase during the glucose-deprivation phase of the experiment and then decrease again during the phase of rescue from glucose deprivation, which demonstrates reversibility of changes in MCT1 expression. Similar trends are observed in the MCT1 mRNA levels of MCF7-sh-WISP2 cells during ‘glucose-deprivation’ and ‘rescue’ experiments, whereas an increase resembling the one detected in the MCT1 protein expression levels is not observed in the MCT2 mRNA levels, and no MCT4 mRNA is detected (cf. Fig.S4 in Sup.Mat.S3). In contrast, no appreciable change in MCT1 expression of MCF7 cells is observed during both ‘glucose-deprivation’ and ‘rescue’ experiments (cf. Fig.S3 in Sup.Mat.S3).

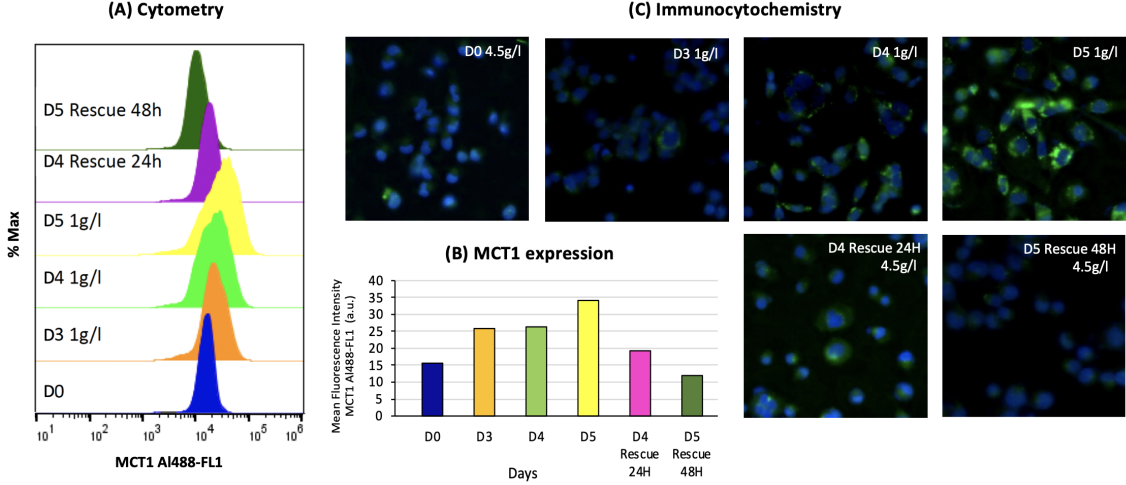


Figure 2: Dynamics of MCT1 expression in ‘glucose-deprivation’ and ‘rescue’ experiments conducted on MCF7-sh-WISP2 cells. (A),(C) MCT1 protein expression of MCF7-sh-WISP2 cells, assessed through flow cytometry analysis (panel (A)) and immunocytochemistry analysis using an MCT1 antibody (green staining in panel (C)), upon seeding (i.e. on day 0) and on days 3-5 of ‘glucose-deprivation’ experiments conducted for five days (sub-panel D0 and sub-panels D3-D5). MCT1 protein expression of MCF7-sh-WISP2 cells during the phase of rescue from glucose deprivation in the corresponding ‘rescue’ experiments (i.e. on days 4 and 5) is also displayed (sub-panels D4 Rescue and D5 Rescue). (B) Mean fluorescence intensity of MCT1 labelling for MCF7-sh-WISP2 cells (in units of 10^3), obtained from the fluorescence intensity distributions of panel (A) plotted on a logarithmic scale.

3.3 Both spontaneous and environment-induced MCT1-expression changes contribute to the adaptation of MCF7-sh-WISP2 cells to glucose deprivation

There is good quantitative agreement between numerical results obtained by simulating ‘glucose-deprivation’ and ‘rescue’ experiments through the calibrated model in which both spontaneous and environment-induced changes in MCT1 expression are included (i.e. $\Phi \neq 0$ and $\Psi^\pm \neq 0$) and experimental observations for MCF7-sh-WISP2 cells deprived of glucose and rescued from glucose deprivation, as shown by the plots in Fig.3, and as additionally highlighted by the high likelihood associated with the obtained OPS (cf. Tab.S1 in Sup.Mat.S2). Instead, levels of intercellular variability in MCT1 expression much higher or lower than those estimated from experimental data are observed in numerical simulations of the experiments carried out through calibrated reduced models that take into account only spontaneous or environment-induced changes in MCT1 expression (i.e. $\Phi \neq 0$ and $\Psi^\pm \equiv 0$ or $\Phi \equiv 0$ and $\Psi^\pm \neq 0$), respectively, as demonstrated by the dynamics of the variance of the MCT1 expression distribution, σ^2 , displayed in Fig.S5(d) in Sup.Mat.S3. Furthermore, the results of numerically simulated ‘glucose-deprivation’ experiments carried out over a time span longer than that of *in vitro* experiments suggest that the synergy between these two forms of changes in MCT1 expression accelerates collective cell adaptation to glucose deprivation, as demonstrated by the fact that, when $\Phi \neq 0$ and $\Psi^\pm \neq 0$, the mean level of MCT1 expression, μ , converges more quickly to the level y_H , which in our modelling framework is the level endowing MCF7-sh-WISP2 cells with the maximum capability of taking lactate from the extracellular environment and reusing it to produce the energy required for their proliferation when glucose is scarce (cf. Fig.S6 in Sup.Mat.S3).

Taken together, these results support the idea that both spontaneous and environment-induced changes in MCT1 expression contribute to the adaptation of MCF7-sh-WISP2 cells to glucose deprivation. In

particular, the modelling assumptions underlying these numerical results provide the following theoretical explanation for the increase in the mean level of MCT1 expression experimentally observed amongst glucose-deprived MCF7-sh-WISP2 cells. Cells with different levels of MCT1 expression emerge as a consequence of spontaneous changes in gene expression due to non-genetic instability. On top of this, as the glucose concentration decreases and the lactate concentration increases during ‘glucose-deprivation’ experiments, environment-induced changes in gene expression mediated by lactate-associated signalling pathways lead cells to express MCT1 at a higher level. Cells with levels of MCT1 expression closer to the fittest one, which in glucose-poor environments is higher than in glucose-rich environments, are then dynamically selected. The interplay between these evolutionary processes results in a progressive increase in the mean level of MCT1 expression of MCF7-sh-WISP2 cells.

3.4 Respective contributions of spontaneous and environment-induced MCT1-expression changes in the adaptation of MCF7-sh-WISP2 cells to glucose deprivation

The analytical results of Proposition S2.1 in Sup.Mat.S2 (cf. Eqs. (S28)₁ and (S28)₂ along with the relations given by Eq.(S4)) clarify how spontaneous and environment-induced changes in gene expression, along with environmental selection on MCT1 expression, affect the dynamics of the mean level of MCT1 expression, μ , and the corresponding variance, σ^2 , in MCF7-sh-WISP2 cells. In summary, larger values of the rate of spontaneous changes in MCT1 expression, Φ , accelerate the growth of σ^2 , while a stronger environmental selection on MCT1 expression (i.e. a larger selection gradient b) leads to reduced values of σ^2 . In turn, larger values of σ^2 enhance the rate at which μ approaches the fittest level of MCT1 expression, Y . Such a rate also increase with the strength of environmental selection on MCT1 expression (i.e. the selection gradient b). Moreover, under glucose deprivation, larger values of the rate at which environment-induced changes lead to an increase in MCT1 expression, Ψ^+ , promote the growth of μ . These analytical results are confirmed by the results of numerical simulations of ‘glucose-deprivation’ experiments presented in Fig.S7 in Sup.Mat.S3, which show that larger values of Φ and Ψ^+ correlate with a faster increase of σ^2 and μ .

Taken together, these results clarify the roles played by spontaneous and environment-induced changes in MCT1 expression in the evolutionary dynamics of glucose-deprived MCF7-sh-WISP2 cells. The former promote intercellular variability in MCT1 expression, which creates the substrate for environmental selection to act upon and speed up the selective sweep underlying collective cell adaptation to glucose deprivation, while the latter triggers a prompt adaptive response of glucose-deprived MCF7-sh-WISP2 cells by promoting overexpression of MCT1. These conclusions are also supported by the fact that estimation of the model parameters from experimental data (cf. the OPS reported in Tab.S1 in Sup.Mat.S2) indicate that the rate of environment-induced changes in the level of MCT1 expression is approximately three orders of magnitude larger than the rate of spontaneous changes.

3.5 Spontaneous MCT1-expression changes may constitute a long-term bet-hedging mechanism for MCF7-sh-WISP2 cells under glucose deprivation

The mathematical model makes it possible to explore the cell evolutionary dynamics beyond timescales and scenarios which can be investigated through experiments. In particular, the analytical results of Theorem S2.2 in Sup.Mat.S2 (cf. Remark S2.3 in Sup.Mat.S2) provide a complete characterisation of the equilibrium values of the number, the mean level of MCT1 expression and the related variance of MCF7-sh-WISP2 cells under virtual scenarios where the glucose and lactate concentrations are kept constant, i.e. a complete characterisation of the limits $\rho(t) \rightarrow \rho_\infty$, $\mu(t) \rightarrow \mu_\infty$ and $\sigma^2(t) \rightarrow \sigma_\infty^2$ as $t \rightarrow \infty$ when $G(t) = \bar{G}$ and $L(t) = \bar{L}$ for all $t \geq 0$. These analytical results are confirmed by the results of numerical simulations of the calibrated model summarised by Fig.S8 in Sup.Mat.S3, which demonstrate that the equilibrium values ρ_∞ , μ_∞ and σ_∞^2 are ultimately attained when $(G(t), L(t)) \equiv (\bar{G}, \bar{L})$.

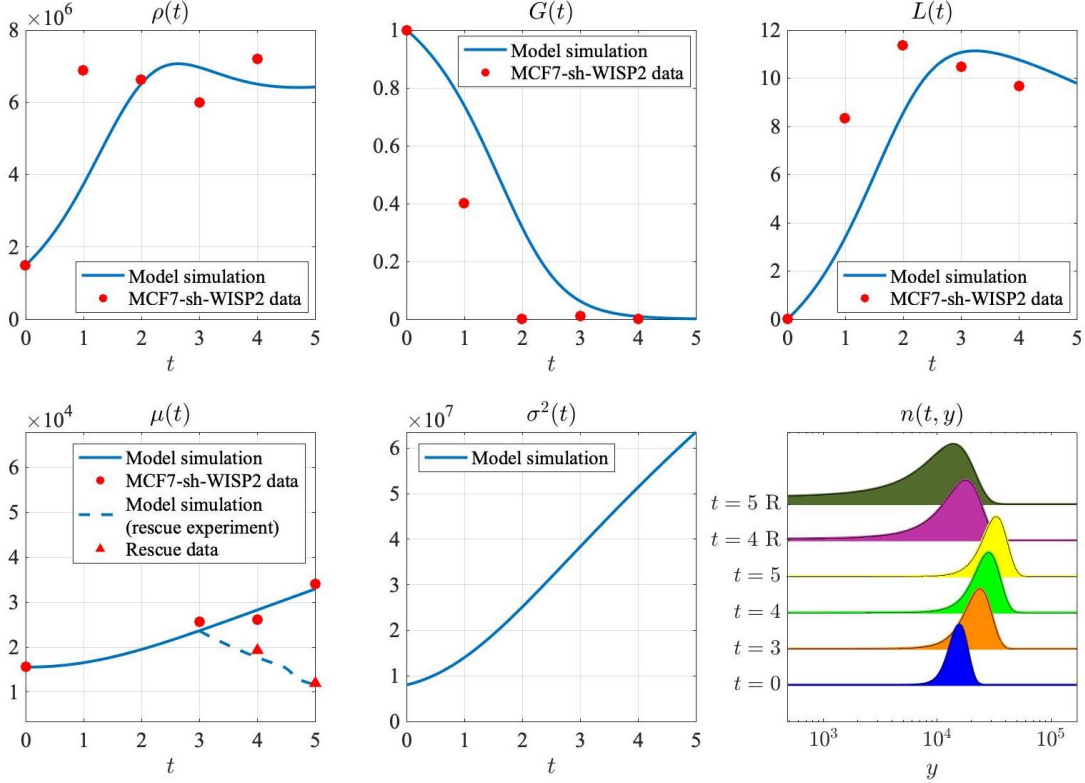


Figure 3: Numerical simulations of ‘glucose-deprivation’ and ‘rescue’ experiments conducted on MCF7-sh-WISP2 cells. Simulated dynamics of the cell number $\rho(t)$ (top-left panel), the glucose concentration $G(t)$ (top-central panel), the lactate concentration $L(t)$ (top-right panel), the mean level of MCT1 expression $\mu(t)$ (bottom-left panel, solid line), the related variance $\sigma^2(t)$ (bottom-central panel), and the MCT1 expression distribution $n(t, y)$ (bottom-right panel, $t = 0$ - $t = 5$) in ‘glucose-deprivation’ experiments conducted on MCF7-sh-WISP2 cells. Numerical simulations were carried out for the calibrated model in which both spontaneous and environment-induced changes in MCT1 expression are included (i.e. $\Phi \not\equiv 0$ and $\Psi^\pm \not\equiv 0$), under the OPS reported in Tab.S1 in Sup.Mat.S2. The MCT1 expression distribution is plotted on the logarithmic scale as for the outputs of flow cytometry analyses to facilitate visual comparison. The MCT1 expression distribution during the phase of rescue from glucose deprivation in the corresponding simulations of ‘rescue’ experiments is also displayed (bottom-right panel, $t = 4$ R and $t = 5$ R) along with the mean level of MCT1 expression (bottom-left panel, dashed line). The red markers highlight experimental data that are used to carry out model calibration, with circles and triangles corresponding to ‘glucose-deprivation’ and ‘rescue’ experiments, respectively. The values of t are in days, the values of $G(t)$ are in g/l, and the values of $L(t)$ are in mmol/l.

The results of Theorem S2.2 complement the results discussed in Sec. 3.3 by showing that the equilibrium value of the variance of the MCT1 expression distribution, σ_∞^2 , increases with the rate of spontaneous changes in MCT1 expression, Φ , and decreases with the strength of environmental selection on MCT1 expression (i.e. the selection gradient b). The results of Theorem S2.2 also demonstrate that when glucose is scarce and lactate is present (i.e. when $\bar{G} < G^*$ and $\bar{L} > 0$), and thus under glucose deprivation, the distance between the equilibrium value of the mean level of MCT1 expression, μ_∞ , and the fittest level of MCT1 expression, Y , increases with the rate at which environment-induced changes lead to an increase in MCT1 expression, Ψ^+ , and decreases with both the rate of spontaneous changes, Φ , and the strength of

environmental selection on MCT1 expression (i.e. the selection gradient b). This supports the idea that, whilst enabling a faster adaptive response to glucose deprivation, as discussed in Sec. 3.4, environment-induced changes in MCT1 expression may ultimately lead to suboptimal adaptation, whereas spontaneous changes may constitute a long-term bet-hedging mechanism.

Moreover, the heat maps in Fig. 4 illustrate how the equilibrium values ρ_∞ , μ_∞ and σ_∞^2 vary with the glucose and lactate concentrations \bar{G} and \bar{L} , under the OPS reported in Tab.S1 in Sup.Mat.S2. In summary, when glucose is scarce (i.e. for $\bar{G} < G^*$ with $G^* \approx 1\text{g/l}$ in the obtained OPS): μ_∞ decreases with \bar{G} and increases with \bar{L} ; σ_∞^2 increases as \bar{G} decreases and reaches maximum levels when \bar{L} is also small; ρ_∞ increases with both \bar{G} and \bar{L} . On the other hand, when the glucose level is sufficiently high (i.e. for $\bar{G} \geq G^*$), μ_∞ drops to y_L and both ρ_∞ and σ_∞^2 vary very little with \bar{G} and \bar{L} – i.e. ρ_∞ remains relatively high and σ_∞^2 remains relatively low.

These findings recapitulate the results of numerical simulations of ‘glucose-deprivation’ and ‘rescue’ experiments displayed in Fig.3 by corroborating the idea that, whereas lower mean levels of MCT1 expression emerge when the concentration of glucose in the extracellular environment is sufficiently high, as in ‘rescue’ experiments, glucose deprivation leads to the selection for cells that are capable of exploiting lactate as an alternative energy source, which results in higher mean levels of MCT1 expression amongst MCF7-sh-WISP2 cells and allows for relatively high cell numbers in spite of glucose scarcity.

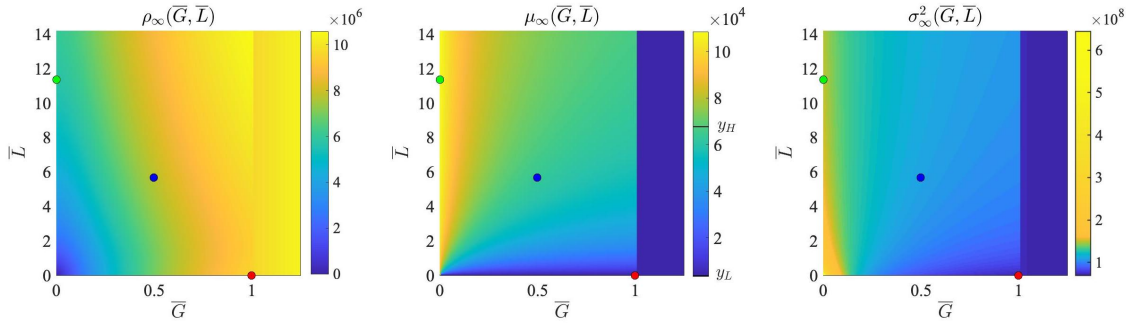


Figure 4: Equilibrium values of the number, the mean level of MCT1 expression and the related variance of MCF7-sh-WISP2 cells predicted by the mathematical model under constant concentrations of glucose and lactate. Plots of the equilibrium number ρ_∞ (left panel), the mean level of MCT1 expression μ_∞ (central panel), and the related variance σ_∞^2 (right panel) of MCF7-sh-WISP2 cells given by Theorem S2.2 in Sup.Mat.S2 (cf. Eq.(S51)) as functions of constant concentrations of glucose and lactate (\bar{G}, \bar{L}) , under the OPS reported in Tab.S1 in Sup.Mat.S2. The green, blue and red dots highlight the values of $(G(t), L(t)) \equiv (\bar{G}, \bar{L})$ that are used to obtain the numerical results of Fig.S8 in Sup.Mat.S3. The values of \bar{G} are in units of g/l , while the values of \bar{L} are in units of mmol/l .

4 Discussion

We adopted an experimentally-informed mathematical modelling approach to investigate the evolutionary dynamics of glucose-deprived cancer cells.

In vitro experiments were conducted on two breast cancer cell lines, MCF7 and MCF7-sh-WISP2, seeded at high cell numbers and quickly consuming the glucose initially available at physiological levels. Experimental outputs revealed that the more aggressive MCF7-sh-WISP2 cells have the ability to survive and sustain substantial proliferation in low-glucose conditions, as opposed to the less aggressive MCF7 cells. Changes in lactate levels *in situ* suggested lactate uptake by MCF7-sh-WISP2 cells, and flow cytometry and immunocytochemistry analyses indicated an associated increase in MCT1 expression, which was then reversed when cells were rescued and exposed again to higher glucose levels.

Experimental data on the MCF7-sh-WISP2 cell line were used to calibrate the proposed mathematical model of cell evolutionary dynamics, and the MCT1 expression distributions obtained through flow cytometry analyses were compared with those predicted by the mathematical model. We found that the calibrated model, whose numerical simulation results are in good quantitative agreement with experimental data, best reproduces experimental observations when the effects of both spontaneous and environment-induced changes in MCT1 expression are taken into account. This finding indicates that cognate studies considering only one of these two types of changes in gene expression may be overestimating the rates at which the considered type of change occurs, overall disregarding the combined effect of the two of them.

The analytical and numerical results of the calibrated model presented here indicate that environment-induced changes in MCT1 expression mediated by lactate-associated signalling pathways enable a prompt adaptive response of glucose-deprived cancer cells. Furthermore, spontaneous changes in MCT1 expression due to non-genetic instability create the substrate for natural selection to act upon, speeding up the selective sweep underlying cancer cell adaptation to glucose deprivation, and may constitute a long-term bet-hedging mechanism. These results on the respective roles played by spontaneous and environment-induced changes in gene expression in the evolutionary dynamics of cancer cells, whilst having been obtained for glucose-deprived cells of the MCF7-sh-WISP2 line, may extend to other cell lines and scenarios whereby changes in gene expression elicit metabolic reprogramming of cancer cells under nutrient deprivation – e.g. HIF1 favouring anaerobic energy pathways or CD36 promoting fatty acid uptake [11, 29, 44].

The optimal parameter set obtained from model calibration suggests that the MCT1 fluorescence intensity levels recorded at the end of the *in vitro* experiments on MCF7-sh-WISP2 cells do not correspond to maximal levels of lactate uptake, and MCT1 expression levels may continue to increase over the span of a month. In practice, performing the experiments over a longer timeframe we expect cells to die out faster than as predicted by the model, due to external factors, demographic stochasticity at low cell numbers or additional byproducts of cell metabolism that are not incorporated into the modelling framework proposed here. Nevertheless, it is evident from our experimental and numerical results that the observed increase in MCT1 expression of MCF7-sh-WISP2 cells over the span of a few days is sufficient to ensure survival and sustain proliferation under glucose deprivation, maintaining the population at high cell numbers for about a week, by the end of which we expect cells to have initiated alternative survival mechanisms associated with disease progression *in vivo* [11, 12].

While we recorded an increase in MCT1 expression of glucose-deprived MCF7-sh-WISP2 cells, no MCT4 mRNA was detected, which suggests that the *in vitro* environmental conditions here investigated do not influence the expression of such a monocarboxylate transporter. It would be relevant to perform similar experiments under hypoxic conditions, as hypoxia-regulated signalling pathways may explain the increase in MCT4 expression observed *in vivo* far from tumour blood vessels. In this regard, it would also be significant to formulate a spatially-explicit extension of the present model where oxygen dependency of various dynamics, here ignored as experiments were carried out in normoxic conditions, was modelled explicitly. Such an extended model would allow for theoretical studies on the still debated role of hypoxia in MCT1 expression at tissue level, which might reconcile reported discrepancies between oxygen and pH profiles [4, 45–47], and could inform anti-cancer therapeutic approaches based on MCT1 blockers [13, 14].

Acknowledgements

The authors acknowledge the valuable assistance of Romain Morichon and Annie Munier of the Sorbonne Université-INSERM, UMR_S938, Centre de Recherche Saint-Antoine Imagery and cytometry platform. T.L. thanks the Istituto Nazionale di Alta Matematica (INdAM) and the Gruppo Nazionale per la Fisica Matematica (GNFM) for their support.

Funding

C.V. has received funding from the European Research Council (ERC) under the European Union’s Horizon 2020 research and innovation programme (grant agreement No 740623). T.L. gratefully acknowledges support from the Italian Ministry of University and Research (MUR) through the grant “Dipartimenti di Eccellenza 2018-2022” (Project no. E11G18000350001) and the PRIN 2020 project (No. 2020JLWP23) “Integrated Mathematical Approaches to Socio-Epidemiological Dynamics” (CUP: E15F21005420006). T.L. and C.V. gratefully acknowledge support of the Institut Henri Poincaré (UAR 839 CNRS-Sorbonne Université), and LabEx CARMIN (ANR-10-LABX-59-01). L.A., T.L. and C.V. gratefully acknowledge support from the CNRS International Research Project ‘Modélisation de la biomécanique cellulaire et tissulaire’ (MOCETIBI).

References

- [1] Susana Romero-Garcia, Jose Sullivan Lopez-Gonzalez, José Luis Béz Viveros, Dolores Aguilar-Cazares, and Heriberto Prado-Garcia. Tumor cell metabolism: an integral view. *Cancer Biology & Therapy*, 12(11):939–948, 2011.
- [2] Joanne R Doherty, John L Cleveland, et al. Targeting lactate metabolism for cancer therapeutics. *The Journal of Clinical Investigation*, 123(9):3685–3692, 2013.
- [3] Juan C García-Cañaveras, Li Chen, and Joshua D Rabinowitz. The tumor metabolic microenvironment: Lessons from lactate. *Cancer Research*, 79(13):3155–3162, 2019.
- [4] Qian Wang, Peter Vaupel, Sibylle I Ziegler, and Kuangyu Shi. Exploring the quantitative relationship between metabolism and enzymatic phenotype by physiological modeling of glucose metabolism and lactate oxidation in solid tumors. *Physics in Medicine & Biology*, 60(6):2547, 2015.
- [5] Douglas Hanahan and Robert A Weinberg. Hallmarks of cancer: the next generation. *Cell*, 144(5):646–674, 2011.
- [6] Luigi Ippolito, Andrea Morandi, Elisa Giannoni, and Paola Chiarugi. Lactate: a metabolic driver in the tumour landscape. *Trends in Biochemical Sciences*, 44(2):153–166, 2019.
- [7] Chongru Zhao, Min Wu, Ning Zeng, Mingchen Xiong, Weijie Hu, Wenchang Lv, Yi Yi, Qi Zhang, and Yiping Wu. Cancer-associated adipocytes: Emerging supporters in breast cancer. *Journal of Experimental & Clinical Cancer Research*, 39(1):1–17, 2020.
- [8] Andrew P Halestrap. Monocarboxylic acid transport. *Comprehensive Physiology*, 3(4):1611–1643, 2013.
- [9] Simon J Park, Chase P Smith, Ryan R Wilbur, Charles P Cain, Sankeerth R Kallu, Srijan Valasapalli, Arpit Sahoo, Maheedhara R Guda, Andrew J Tsung, and Kiran K Velpula. An overview of MCT1 and MCT4 in GBM: small molecule transporters with large implications. *American Journal of Cancer Research*, 8(10):1967, 2018.
- [10] Pierre Sonveaux, Frédérique Végran, Thies Schroeder, Melanie C Wergin, Julien Verrax, Zahid N Rabbani, Christophe J De Saedeleer, Kelly M Kennedy, Caroline Diepart, Bénédicte F Jordan, et al. Targeting lactate-fueled respiration selectively kills hypoxic tumor cells in mice. *The Journal of Clinical Investigation*, 118(12):3930–3942, 2008.
- [11] Baoyi Liu and Xin Zhang. Metabolic reprogramming underlying brain metastasis of breast cancer. *Frontiers in Molecular Biosciences*, 8, 2021.

- [12] Alpaslan Tasdogan, Brandon Faubert, Vijayashree Ramesh, Jessalyn M Ubellacker, Bo Shen, Ashley Solmonson, Malea M Murphy, Zhimin Gu, Wen Gu, Misty Martin, et al. Metabolic heterogeneity confers differences in melanoma metastatic potential. *Nature*, 577(7788):115–120, 2020.
- [13] Cyril Corbet, Estelle Bastien, Nihed Draoui, Bastien Doix, Lionel Mignion, Bénédicte F Jordan, Arnaud Marchand, Jean-Christophe Vanherck, Patrick Chaltin, Olivier Schakman, et al. Interruption of lactate uptake by inhibiting mitochondrial pyruvate transport unravels direct antitumor and radiosensitizing effects. *Nature Communications*, 9(1):1–11, 2018.
- [14] Zi-Hao Wang, Wen-Bei Peng, Pei Zhang, Xiang-Ping Yang, and Qiong Zhou. Lactate in the tumour microenvironment: From immune modulation to therapy. *EBioMedicine*, 73:103627, 2021.
- [15] Lucia Longhitano, Nunzio Vicario, Daniele Tibullo, Cesarina Giallongo, Giuseppe Broggi, Rosario Caltabiano, Giuseppe Maria Vincenzo Barbagallo, Roberto Altieri, Marta Baghini, Michelino Di Rosa, et al. Lactate induces the expressions of MCT1 and HCAR1 to promote tumor growth and progression in glioblastoma. *Frontiers in Oncology*, 12, 2022.
- [16] Sui Huang. Genetic and non-genetic instability in tumor progression: link between the fitness landscape and the epigenetic landscape of cancer cells. *Cancer and Metastasis Reviews*, 32(3):423–448, 2013.
- [17] Amy Brock, Hannah Chang, and Sui Huang. Non-genetic heterogeneity – a mutation-independent driving force for the somatic evolution of tumours. *Nature Reviews Genetics*, 10(5):336–342, 2009.
- [18] Garth L Nicolson. Tumor cell instability, diversification, and progression to the metastatic phenotype: from oncogene to oncofetal expression. *Cancer Research*, 47(6):1473–1487, 1987.
- [19] Kasper Daniel Hansen, Winston Timp, Héctor Corrada Bravo, Sarven Sabunciyan, Benjamin Langmead, Oliver G McDonald, Bo Wen, Hao Wu, Yun Liu, Dinh Diep, et al. Increased methylation variation in epigenetic domains across cancer types. *Nature Genetics*, 43(8):768–775, 2011.
- [20] Juan Sandoval and Manel Esteller. Cancer epigenomics: beyond genomics. *Current Opinion in Genetics & Development*, 22(1):50–55, 2012.
- [21] Gabriele Berger and Sarah-Maria Fendt. The metabolism of cancer cells during metastasis. *Nature Reviews Cancer*, 21(3):162–180, 2021.
- [22] Di Zhang, Zhanyun Tang, He Huang, Guolin Zhou, Chang Cui, Yeing Weng, Wenchao Liu, Sunjoo Kim, Sangkyu Lee, Mathew Perez-Neut, et al. Metabolic regulation of gene expression by histone lactylation. *Nature*, 574(7779):575–580, 2019.
- [23] Aleksandra Ardaševa, Robert A. Gatenby, Alexander R. A. Anderson, Helen M. Byrne, Philip K. Maini, and Tommaso Lorenzi. A mathematical dissection of the adaptation of cell populations to fluctuating oxygen levels. *Bulletin of Mathematical Biology*, 82(6):81, 2020.
- [24] Giulia L Celora, Samuel B Bader, Ester M Hammond, Philip K Maini, Joe M Pitt-Francis, and Helen M Byrne. A DNA-structured mathematical model of cell-cycle progression in cyclic hypoxia. *Journal of Theoretical Biology*, 545:111104, 2022.
- [25] Heyrim Cho and Doron Levy. Modeling the dynamics of heterogeneity of solid tumors in response to chemotherapy. *Bulletin of Mathematical Biology*, 79(12):2986–3012, 2017.
- [26] Giada Fiandaca, Marcello Delitala, and Tommaso Lorenzi. A mathematical study of the influence of hypoxia and acidity on the evolutionary dynamics of cancer. *Bulletin of Mathematical Biology*, 83(7):1–29, 2021.

- [27] Tommaso Lorenzi, Chandrasekhar Venkataraman, Alexander Lorz, and Mark AJ Chaplain. The role of spatial variations of abiotic factors in mediating intratumour phenotypic heterogeneity. *Journal of Theoretical Biology*, 451:101–110, 2018.
- [28] Alexander Lorz, Tommaso Lorenzi, Jean Clairambault, Alexandre Escargueil, and Benoît Perthame. Modeling the effects of space structure and combination therapies on phenotypic heterogeneity and drug resistance in solid tumors. *Bulletin of Mathematical Biology*, 77(1):1–22, 2015.
- [29] Chiara Villa, Mark A Chaplain, and Tommaso Lorenzi. Modeling the emergence of phenotypic heterogeneity in vascularized tumors. *SIAM Journal on Applied Mathematics*, 81(2):434–453, 2021.
- [30] Chiara Villa, Mark AJ Chaplain, and Tommaso Lorenzi. Evolutionary dynamics in vascularised tumours under chemotherapy: Mathematical modelling, asymptotic analysis and numerical simulations. *Vietnam Journal of Mathematics*, 49(1):143–167, 2021.
- [31] Jessica B McGillen, Catherine J Kelly, Alicia Martínez-González, Natasha K Martin, Eamonn A Gaffney, Philip K Maini, and Víctor M Pérez-García. Glucose–lactate metabolic cooperation in cancer: Insights from a spatial mathematical model and implications for targeted therapy. *Journal of Theoretical Biology*, 361:190–203, 2014.
- [32] Berta Mendoza-Juez, Alicia Martínez-González, Gabriel F Calvo, and Víctor M Pérez-García. A mathematical model for the glucose-lactate metabolism of in vitro cancer cells. *Bulletin of Mathematical Biology*, 74(5):1125–1142, 2012.
- [33] Nathaniel J Linden, Boris Kramer, and Padmini Rangamani. Bayesian parameter estimation for dynamical models in systems biology. *bioRxiv*, 2022.
- [34] Ruben Martinez-Cantin. BayesOpt: a Bayesian optimization library for nonlinear optimization, experimental design and bandits. *Journal of Machine Learning Research*, 15(1):3735–3739, 2014.
- [35] In Jae Myung. Tutorial on maximum likelihood estimation. *Journal of Mathematical Psychology*, 47(1):90–100, 2003.
- [36] Nathalie Ferrand, Anne Gnanapragasam, Guillaume Dorothee, Gérard Redeuilh, Annette K Larsen, and Michèle Sabbah. Loss of WISP2/CCN5 in estrogen-dependent MCF7 human breast cancer cells promotes a stem-like cell phenotype. *PloS One*, 9(2):e87878, 2014.
- [37] Michèle Sabbah, Céline Prunier, Nathalie Ferrand, Virginie Megalophonos, Kathleen Lambein, Olivier De Wever, Nicolas Nazaret, Joël Lachuer, Sylvie Dumont, and Gérard Redeuilh. CCN5, a novel transcriptional repressor of the transforming growth factor β signaling pathway. *Molecular and Cellular Biology*, 31(7):1459–1469, 2011.
- [38] Rebecca H Chisholm, Tommaso Lorenzi, Alexander Lorz, Annette K Larsen, Luis Almeida, Alexandre Escargueil, and Jean Clairambault. Emergence of drug tolerance in cancer cell populations: an evolutionary outcome of selection, non-genetic instability and stress-induced adaptation. *Cancer Research*, 75(6):930–939, 2015.
- [39] Tommaso Lorenzi, Rebecca H Chisholm, and Jean Clairambault. Tracking the evolution of cancer cell populations through the mathematical lens of phenotype-structured equations. *Biology Direct*, 11(1):43, 2016.
- [40] Luís Almeida, Patrizia Bagnerini, Giulia Fabrini, Barry D Hughes, and Tommaso Lorenzi. Evolution of cancer cell populations under cytotoxic therapy and treatment optimisation: insight from a phenotype-structured model. *ESAIM: Mathematical Modelling and Numerical Analysis*, 53(4):1157–1190, 2019.

- [41] Aleksandra Ardaševa, Robert A Gatenby, Alexander RA Anderson, Helen M Byrne, Philip K Maini, and Tommaso Lorenzi. Evolutionary dynamics of competing phenotype-structured populations in periodically fluctuating environments. *Journal of Mathematical Biology*, 80(3):775–807, 2020.
- [42] Rebecca H Chisholm, Tommaso Lorenzi, Laurent Desvillettes, and Barry D Hughes. Evolutionary dynamics of phenotype-structured populations: from individual-level mechanisms to population-level consequences. *Zeitschrift für angewandte Mathematik und Physik*, 67(4):1–34, 2016.
- [43] Tommaso Lorenzi, Rebecca H Chisholm, Laurent Desvillettes, and Barry D Hughes. Dissecting the dynamics of epigenetic changes in phenotype-structured populations exposed to fluctuating environments. *Journal of Theoretical Biology*, 386:166–176, 2015.
- [44] Maurice Zaoui, Mehdi Morel, Nathalie Ferrand, Soraya Fellahi, Jean-Philippe Bastard, Antonin Lamazière, Annette Kragh Larsen, Véronique Béréziat, Michael Atlan, and Michèle Sabbah. Breast-associated adipocytes secretome induce fatty acid uptake and invasiveness in breast cancer cells via CD36 independently of body mass index, menopausal status and mammary density. *Cancers*, 11(12):2012, 2019.
- [45] Gabriel Helmlinger, Fan Yuan, Marc Dellian, and Rakesh K Jain. Interstitial pH and pO₂ gradients in solid tumors *in vivo*: high-resolution measurements reveal a lack of correlation. *Nature Medicine*, 3(2):177–182, 1997.
- [46] Vera Miranda-Gonçalves, Sara Granja, Olga Martinho, Mrinalini Honavar, Marta Pojo, Bruno M Costa, Manuel M Pires, Célia Pinheiro, Michelle Cordeiro, Gil Bebiano, et al. Hypoxia-mediated upregulation of MCT1 expression supports the glycolytic phenotype of glioblastomas. *Oncotarget*, 7(29):46335, 2016.
- [47] Mohammed S Ullah, Andrew J Davies, and Andrew P Halestrap. The plasma membrane lactate transporter MCT4, but not MCT1, is up-regulated by hypoxia through a HIF-1 α -dependent mechanism. *Journal of Biological Chemistry*, 281(14):9030–9037, 2006.

Evolutionary dynamics of glucose-deprived cancer cells: insights from experimentally-informed mathematical modelling*

Supplementary Material

Luis Almeida Jérôme Denis Nathalie Ferrand Tommaso Lorenzi[†]

Michéle Sabbah Chiara Villa[‡]

June 12, 2025

S1 Mathematical model

Building on the modelling strategies presented in [6, 10], we develop a mathematical model that describes the evolutionary dynamics of a population of MCF7-sh-WISP2 cells, structured by the level of MCT1 expression, under the environmental conditions determined by the levels of glucose and lactate in the extracellular environment.

S1.1 Preliminaries

We introduce the cell population density function $n(t, y)$, which represents the number of MCF7-sh-WISP2 cells with level of MCT1 expression $y \in \mathbb{R}$ at time $t \in \mathbb{R}_+$ (i.e. the MCT1 expression distribution of MCF7-sh-WISP2 cells at time t). The cell number, the mean level of MCT1 expression and the related variance, which provides a possible measure for the level of intercellular variability in MCT1 expression, are then computed, respectively, as

$$\rho(t) = \int_{\mathbb{R}} n(t, y) \, dy, \quad \mu(t) = \frac{1}{\rho(t)} \int_{\mathbb{R}} y n(t, y) \, dy, \quad \sigma^2(t) = \frac{1}{\rho(t)} \int_{\mathbb{R}} y^2 n(t, y) \, dy - \mu^2(t). \quad (\text{S1})$$

We also introduce the functions $G(t)$ and $L(t)$, which model, respectively, the concentrations of glucose and lactate in the extracellular environment.

The results of *in vitro* experiments (cf. Sec. 3.2 in the Main Manuscript) indicate that the MCT1 expression distribution of MCF7-sh-WISP2 cells is, to a first approximation, unimodal with a single peak at the centre of the distribution. The location of the centre of the distribution moves from lower to higher expression levels when cells experience glucose deprivation and from higher to lower expression levels when cells are rescued from glucose deprivation. Hence, we assume that there is a level of MCT1 expression (i.e. the fittest level of MCT1 expression) endowing cells with the highest fitness depending on the environmental conditions determined by the concentrations of glucose and lactate. Moreover, the results of *in vitro* experiments (cf. Sec. 3.1 in the Main Manuscript) support the idea that proliferation and survival of MCF7-sh-WISP2 cells correlate with glucose uptake when glucose levels are sufficiently high and with lactate uptake when glucose levels are low. Therefore, we further assume that there are

*This paper is submitted for publication

[†]Corresponding author affiliation and email: Department of Mathematical Sciences “G. L. Lagrange”, Dipartimento di Eccellenza 2018-2022, Politecnico di Torino, 10129 Torino, Italy - tommaso.lorenzi@polito.it

[‡]Corresponding author affiliation and email: Sorbonne Université, CNRS, Université de Paris, Inria, Laboratoire Jacques-Louis Lions UMR 7598, 75005 Paris, France - chiara.villa.1@sorbonne-universite.fr

a level of MCT1 expression, y_L , endowing cells with the highest rate of proliferation via glycolysis and a higher level of MCT1 expression, $y_H > y_L$, endowing cells with the highest rate of proliferation via lactate reuse when glucose is scarce – i.e. if the concentration of glucose in the extracellular environment is lower than a threshold level G^* above which cells stop taking lactate from the extracellular environment in order to prioritise glucose uptake. We then introduce the following change of variable

$$x = \frac{y - y_L}{y_H - y_L}, \quad (\text{S2})$$

so that the rescaled level of MCT1 expression $x = 0$ corresponds to the level of MCT1 expression $y = y_L$ and the rescaled level of MCT1 expression $x = 1$ corresponds to the level of MCT1 expression $y = y_H$. Under the change of variable defined by Eq. (S2), representing the rescaled MCT1 expression distribution of MCF7-sh-WISP2 cells at time t by the cell population density function $n_r(t, x) = (y_H - y_L) n(t, y)$, we compute the cell number, the mean rescaled level of MCT1 expression and the related variance, respectively, as

$$\rho_r(t) = \int_{\mathbb{R}} n_r(t, x) dx, \quad \mu_r(t) = \frac{1}{\rho_r(t)} \int_{\mathbb{R}} x n_r(t, x) dx, \quad \sigma_r^2(t) = \frac{1}{\rho_r(t)} \int_{\mathbb{R}} x^2 n_r(t, x) dx - \mu_r^2(t). \quad (\text{S3})$$

Remark S1.1 Note that the following relations hold between the quantities defined via Eq. (S3) and Eq. (S1):

$$\rho(t) = \rho_r(t), \quad \mu(t) = y_L + \mu_r(t)(y_H - y_L), \quad \sigma^2(t) = \sigma_r^2(t)(y_H - y_L)^2. \quad (\text{S4})$$

S1.2 Cell dynamics

The dynamics of the population density function $n_r(t, x)$ is governed by the following partial integro-differential equation (PIDE)

$$\begin{cases} \frac{\partial n_r}{\partial t} - \Phi(G(t), L(t)) \frac{\partial^2 n_r}{\partial x^2} + \Psi(G(t), L(t), \mu_r(t)) \frac{\partial n_r}{\partial x} = R(x, G(t), L(t), \rho_r(t)) n_r, & x \in \mathbb{R} \\ \rho_r(t) = \int_{\mathbb{R}} n_r(t, x) dx, \quad \mu_r(t) = \frac{1}{\rho_r(t)} \int_{\mathbb{R}} x n_r(t, x) dx, \end{cases} \quad (\text{S5})$$

where:

- the diffusion term $\Phi(G, L) \frac{\partial^2 n_r}{\partial x^2}$ models the effects of spontaneous changes in MCT1 expression due to non-genetic instability;
- the advection term $\Psi(G, L, \mu_r) \frac{\partial n_r}{\partial x}$ models the effects of environment-induced changes in MCT1 expression mediated by lactate-associated signalling pathways;
- the reaction term $R(x, G, L, \rho_r) n_r$ models the effects of cell proliferation and death under environmental selection on MCT1 expression.

The modelling assumptions underlying the PIDE (S5) are described in the following.

Modelling cell proliferation and death under environmental selection on MCT1 expression

The fitness of cells with rescaled level of MCT1 expression x at time t is modelled by the function

$$R(x, G, L, \rho_r) = p(x, G, L) - d \rho_r. \quad (\text{S6})$$

Definition (S6) translates in mathematical terms to the following biological ideas: all else being equal, cells die due to intracellular competition at rate $d \rho_r$, with the parameter $d > 0$ being related to the

carrying capacity of the *in vitro* system in which the cells are contained; cells with the rescaled level of MCT1 expression x proliferate and die under environmental selection on MCT1 expression at rate $p(x, G, L)$ (i.e. the function p is a net proliferation rate). Based on the considerations and assumptions introduced in Sec. S1.1, we define

$$p(x, G, L) = p_G(x, G) + p_L(x, G, L) \quad (\text{S7})$$

with

$$p_G(x, G) = \gamma_G U_G(G) (1 - x^2), \quad p_L(x, G, L) = \gamma_L U_L(G, L) \left[1 - (1 - x)^2 \right], \quad (\text{S8})$$

$$U_G(G) = \frac{G^m}{(\alpha_G)^m + G^m} \quad \text{and} \quad U_L(G, L) = (1 - H(G - G^*)) \frac{L^c}{(\alpha_L)^c + L^c}. \quad (\text{S9})$$

The function p_G models the net rate of cell proliferation via glycolysis and the function p_L models the net rate of cell proliferation via lactate reuse. The fact that these functions are negative for values of x sufficiently far from 0 (i.e. the rescaled level of MCT1 expression endowing cells with the highest rate of proliferation via glycolysis) and 1 (i.e. the rescaled level of MCT1 expression endowing cells with the highest rate of proliferation via lactate reuse when glucose is scarce) captures the idea that cells with less fit levels of MCT1 expression are driven to extinction by environmental selection. Moreover, the functions U_G and U_L model glucose and lactate uptake, respectively. In the definitions given by Eqs. (S8) and (S9):

- $H(G - G^*)$ is the Heaviside step function centred at the threshold level of glucose G^* (i.e. the level of glucose above which cells stop taking lactate from the extracellular environment and reusing it to produce energy for fuelling their proliferation), that is,

$$H(G - G^*) = \begin{cases} 0, & \text{if } G < G^* \\ 1, & \text{if } G \geq G^*; \end{cases} \quad (\text{S10})$$

- $\gamma_G > 0$ and $\gamma_L > 0$ are the maximum rates of cell proliferation via glycolysis and lactate reuse;
- $\alpha_G > 0$ and $\alpha_L > 0$ are the glucose and lactate concentrations at half receptor occupancy [14];
- $m > 0$ and $c > 0$ are the Hill coefficients for glucose and lactate ligand-receptor dynamics [14].

Under the definitions given by Eq. (S8), after a little algebra, the definition given by Eq. (S7) can be rewritten as

$$p(x, G, L) = a(G, L) - b(G, L) (x - X(G, L))^2 \quad (\text{S11})$$

with

$$a(G, L) = \gamma_G U_G(G) + \frac{(\gamma_L U_L(G, L))^2}{\gamma_G U_G(G) + \gamma_L U_L(G, L)}, \quad b(G, L) = \gamma_L U_L(G, L) + \gamma_G U_G(G) \quad (\text{S12})$$

and

$$X(G, L) = \frac{\gamma_L U_L(G, L)}{\gamma_G U_G(G) + \gamma_L U_L(G, L)}. \quad (\text{S13})$$

Under the environmental conditions defined by the concentrations of glucose G and lactate L : $X(G, L)$ represents the fittest rescaled level of MCT1 expression; $a(G, L)$ is the corresponding maximum fitness (i.e. the proliferation rate of cells exhibiting the fittest rescaled level of MCT1 expression); $b(G, L)$ can be seen as a nonlinear selection gradient that quantifies the strength of environmental selection on MCT1 expression.

Remark S1.2 Note that the definition given by Eq. (S13) implies that $0 \leq X(G, L) \leq 1$ for all $G \geq 0$ and $L \geq 0$. In particular, coherently with the considerations and assumptions introduced in Sec. S1.1, under this definition and the definitions given by Eq. (S9), we have that if $G = 0$ then $X(G, L) = 1$ for any $L > 0$, while if $G \geq G^*$ then $X(G, L) = 0$ for any $L \geq 0$.

Remark S1.3 The fittest level of MCT1 expression, $Y(G, L)$, is obtained from the definition of the fittest rescaled level of MCT1 expression, $X(G, L)$, given by Eq. (S13) through the change of variable defined by Eq. (S2), that is,

$$Y(G, L) = y_L + X(G, L)(y_H - y_L) = y_L + \frac{\gamma_L U_L(G, L)}{\gamma_G U_G(G) + \gamma_L U_L(G, L)}(y_H - y_L). \quad (\text{S14})$$

Modelling spontaneous and environment-induced changes in MCT1 expression

The rate of spontaneous changes in MCT1 expression due to non-genetic instability is modelled by the function

$$\Phi(G, L) = \beta(1 + \zeta U_L(G, L)), \quad (\text{S15})$$

where the lactate uptake function U_L is defined via Eq. (S9). Under the definition given by Eq. (S15), the minimum rate of phenotypic changes due to non-genetic instability, $\beta > 0$, is increased proportionally to lactate uptake with constant of proportionality $\zeta > 0$. This translates in mathematical terms to the idea that, since lactate has been shown to be responsible for histone modifications [3, 17], the effect of non-genetic instability may be enhanced under glucose-deprivation.

Moreover, the rate of environment-induced changes in MCT1 expression mediated by lactate-associated signalling pathways is modelled by the function

$$\Psi(G, L, \mu_r) = \Psi^+(G, L) - \Psi^-(G, \mu_r), \quad (\text{S16})$$

with

$$\Psi^+(G, L) = \lambda_L U_L(G, L) \quad \text{and} \quad \Psi^-(G, \mu_r) = \lambda_G H(G - G^*) (\mu_r)_+, \quad (\text{S17})$$

where the lactate uptake function U_L is defined via Eq. (S9), while $H(G - G^*)$ is the Heaviside step function defined via Eq. (S10). The definitions given by Eqs. (S16) and (S17) translate in mathematical terms the idea that environment-induced changes mediated by lactate-associated signalling pathways lead to: an increase in MCT1 expression at rate Ψ^+ , which is proportional to lactate uptake, under glucose deprivation (i.e. when $G < G^*$); to a decrease in MCT1 expression at rate Ψ^- when the glucose level is sufficiently high (i.e. when $G \geq G^*$). The parameters $\lambda_L > 0$ and $\lambda_G > 0$ model the corresponding maximum rates of environment-induced increase and decrease in MCT1 expression. Moreover, the dependence of Ψ^- on $(\mu_r)_+ = \max\{0, \mu_r\}$ captures the fact that interruption of lactate-associated signalling pathways may occur when $G \geq G^*$ if the mean rescaled level of MCT1 expression of the cells is below the fittest level $x = 0$ (cf. Remark S1.2).

S1.3 Glucose and lactate dynamics

The dynamic of the glucose concentration $G(t)$ is governed by the following ordinary differential equation (ODE)

$$\frac{dG}{dt} = -k_G U_G(G) \rho_r(t), \quad (\text{S18})$$

where the glucose uptake function U_G is defined via Eq. (S9). The ODE (S18) relies on the assumption that glucose is consumed by the cells at a rate proportional to glucose uptake, with constant of proportionality $k_G > 0$. Moreover, the dynamic of the lactate concentration $L(t)$ is governed by the following ODE

$$\frac{dL}{dt} = k_L U_G(G) \rho_r(t) - \eta_L \int_{\mathbb{R}} (p_L(x, G, L))_+ n_r(t, x) dx, \quad (\text{S19})$$

where $(p_L)_+ = \max\{0, p_L\}$, with p_L being the function that models the net rate of cell proliferation via lactate reuse, which is defined via Eq. (S8). Based on earlier studies indicating that most tumours release lactate in quantities linearly related to glucose consumption [15], and coherently with the way in which the effect of glucose consumption is incorporated into the ODE (S18), the ODE (S19) relies on the assumption that lactate is produced by the cells at a rate proportional to glucose uptake, with constant

of proportionality $k_L > 0$. Moreover, the ODE (S19) relies on the additional assumption that lactate is absorbed only by the cells whose rescaled levels of MCT1 expression make them capable of reusing lactate to produce the energy required for their proliferation when glucose is scarce (i.e. cells with rescaled levels of MCT1 expression x corresponding to positive values of $p_L(x, G, L)$), which absorb lactate at a rate proportional to their net proliferation rate, with constant of proportionality (i.e. conversion factor for lactate consumption) $\eta_L > 0$.

S1.4 Initial conditions

Informed by the experimental data reported in Fig.2(A) in the Main Manuscript, we define the initial MCT1 expression distribution of MCF7-sh-WISP2 cells as

$$n(0, y) = n_0(y) \quad \text{with} \quad n_0(y) = \frac{\rho_0}{\sqrt{2\pi\sigma_0^2}} \exp\left(-\frac{(y - \mu_0)^2}{2\sigma_0^2}\right), \quad (\text{S20})$$

where the initial cell number, ρ_0 , the initial mean level of MCT1 expression, μ_0 , and the related variance, σ_0^2 , are defined as

$$\rho_0 = 1.5 \times 10^6, \quad \mu_0 = 15.57 \times 10^3, \quad \sigma_0^2 = 8 \times 10^6. \quad (\text{S21})$$

Hence, under the change of variable defined by Eq. (S2), the initial rescaled MCT1 expression distribution of MCF7-sh-WISP2 cells is

$$n_r(0, x) = n_{r0}(x) \quad \text{with} \quad n_{r0}(x) = \frac{\rho_{r0}}{\sqrt{2\pi\sigma_{r0}^2}} \exp\left(-\frac{(x - \mu_{r0})^2}{2\sigma_{r0}^2}\right), \quad (\text{S22})$$

where (cf. the relations given by Eq. (S4))

$$\rho_{r0} = \rho_0, \quad \mu_{r0} = \frac{\mu_0 - y_L}{y_H - y_L}, \quad \sigma_{r0}^2 = \frac{\sigma_0^2}{(y_H - y_L)^2}. \quad (\text{S23})$$

Remark S1.4 Note that under the relations given by Eq. (S23), we have that $n_{r0}(x)$ in Eq. (S22) and $n_0(y)$ in Eq. (S20) are related by $n_{r0}(x) = (y_H - y_L)n_0(y)$, i.e. we retrieve the relation between $n_r(t, x)$ and $n(t, y)$ introduced in Sec.S1.1.

Moreover, in order to match the experimental data reported in Fig.1(B) in the Main Manuscript, we define the initial concentrations of glucose and lactate, respectively, as

$$G(0) = G_0, \quad L(0) = L_0 \quad \text{with} \quad G_0 = 1 \quad \text{and} \quad L_0 = 0, \quad (\text{S24})$$

where the value of G_0 is in units of g/l and the value of L_0 is in units of mmol/l.

S1.5 Parameter values

The values of the model parameters obtained from experimental data on MCF7-sh-WISP2 cells, through the calibration procedure detailed in Section S2, are summarised in Tab. S1.

S2 Further details of materials and methods

S2.1 *In vitro* experiments

Two breast cancer cell lines are considered: MCF7 (human breast cancer cell line, epithelial phenotype) and MCF7-sh-WISP2 (MCF7 cells invalidated for WISP2 by sh-RNA plasmid, mesenchymal phenotype) [7, 8].

S2.1.1 Cell proliferation and death

Cells were routinely maintained in Dulbecco's modified Eagle medium containing 4.5g/l of glucose supplemented with 10% fetal bovine serum (FBS), L-Glutamine, and antibiotics. For assessing cell proliferation and death, cells were cultured for four days in a medium initially containing 1g/l of glucose. Viable cells were identified via trypan blue exclusion and counted using Beckman Coulter, while cell death was quantified via annexin V-FITC apoptosis staining.

S2.1.2 Flow cytometry analysis

Cells were stained with fluorochrome-conjugated monoclonal antibodies against human MCT1-FITC (Beckman Coulter) at room temperature in the dark for 20 minutes. Cells were then washed with PBS containing 0.5% serum and flow cytometry analysis was carried out. The labelled cells were analysed on a FACS Gallios (Beckman Coulter) and data analysis was performed using the Kaluza software.

S2.1.3 Immunofluorescence staining

Cells were plated on chamber slides and fixed in 4% paraformaldehyde. Cells were stained with anti-MCT1 antibody and secondary anti-Rabbit FITC-conjugated antibody (Jackson ImmunoResearch, Cambridgeshire, UK). After immunolabelling, cells were washed, stained with 1 μ g/mL DAPI (Sigma), and observed by fluorescence microscopy (BX61, Olympus).

S2.1.4 Real-time RT-qPCR

Total RNA was extracted from cell samples using the TRIzol[®] RNA purification reagent. RNA quantity and purity were assessed by using a Spectrophotometer DS-11 (Denovix, Wilmington, DE, USA). One microgram of total RNA from each sample was reverse transcribed, and real-time RT-qPCR measurements were performed as described in [7], using an apparatus Aria MX (Agilent Technologies, Santa Clara, CA, USA) with the corresponding SYBR[®] Green kit, according to the PROMEGA manufacturer's recommendations.

S2.2 Model calibration with experimental data

Experimental data on MCF7-sh-WISP2 cells are used to carry out model calibration through a likelihood-maximising method [9, 12, 13]. First, both the data and the mathematical model, which comprises the PIDE-ODE system (S5), (S18), (S19) subject to the initial conditions defined via Eqs. (S22)-(S24), are nondimensionalised through the procedure summarised in Sec.S2.2.1, to avoid calibration bias. Then, the optimal parameter set (OPS) is obtained by maximising the likelihood, through an iterative process described in Sec.S2.2.2. At each iteration, we solve numerically the nondimensional model, using methods analogous to those described in Sec.S2.4. The MATLAB source code along with the data used for model calibration have been made available on GitHub¹. The obtained OPSs are reported in Tab.S1.

S2.2.1 Nondimensionalisation of the model and data underlying the calibration procedure

Nondimensional model. Let $\hat{t} = t/\tau$, $\hat{n} = n/P^M$, $\hat{G} = G/G^M$ and $\hat{L} = L/L^M$, where we choose $\tau = 1\text{day}$ as reference timescale, and $P^M = 7.195 \times 10^6\text{cells}$, $G^M = 1\text{g/l}$ and $L^M = 11.35\text{mmol/l}$ are, respectively, the maximum cell number, glucose and lactate concentrations recorded during 'glucose-deprivation' experiments. Thus we have the following nondimensional parameters

$$\begin{aligned} \hat{\beta} &= \beta\tau, & \hat{\zeta} &\equiv \zeta, & \hat{\lambda}_L &= \lambda_L\tau, & \hat{\lambda}_G &= \lambda_G\tau, & \hat{\gamma}_G &= \gamma_G\tau, & \hat{\gamma}_L &= \gamma_L\tau, & \hat{\alpha}_G &= \frac{\alpha_G}{G^M}, & \hat{\alpha}_L &= \frac{\alpha_L}{L^M}, \\ \hat{c} &\equiv c, & \hat{m} &\equiv m, & \hat{d} &= d\tau P^M, & \hat{\kappa}_G &= \frac{\kappa_G\tau P^M}{G^M}, & \hat{\kappa}_L &= \frac{\kappa_L\tau P^M}{L^M}, & \hat{\eta}_L &= \frac{\eta_L P^M}{L^M}, & \hat{G}^* &= \frac{G^*}{G^M}. \end{aligned}$$

¹<https://github.com/ChiaraVilla/AlmeidaEtAl2023Evolutionary>

The corresponding initial conditions of the nondimensional model are

$$\hat{n}_{r0}(x) = \frac{\hat{\rho}_{r0}}{\sqrt{2\pi\sigma_{r0}^2}} \exp\left(-\frac{(x - \mu_{r0})^2}{2\sigma_{r0}^2}\right) \quad \text{with} \quad \hat{\rho}_{r0} = 1, \quad \hat{G}(0) = 1 \quad \text{and} \quad \hat{L}(0) = 0,$$

with μ_{r0} and σ_{r0}^2 given by (S23).

Nondimensional data. Let $S_D = \{u_D^i, i = 1, \dots, M\}$ indicate the set of M data points u_D^i , i.e. the experimentally obtained summary statistics. We normalise the MCT1 fluorescence intensity levels recorded during the experiments by means of the transformation defined by Eq. (S2), while the cell numbers and the glucose and lactate concentrations recorded are nondimensionalised, and normalised, by P^M , G^M and L^M introduced above, respectively. We denote the set of M nondimensionalised data points \hat{u}_D^i by $\hat{S}_D = \{\hat{u}_D^i, i = 1, \dots, M\}$.

Nondimensional summary statistics. Let $\hat{S}_P \in \Omega \subset \mathbb{R}_{\geq 0}^N$ indicate the set of nondimensional parameter values in the N -dimensional and bounded parameter space Ω . Solving numerically the nondimensional model employing methods analogous to those described in Sec.S2.4, we obtain the M nondimensional summary statistics $\{\hat{u}_P^i, i = 1, \dots, M\}$, corresponding to the data $\{\hat{u}_D^i, i = 1, \dots, M\}$, predicted by the model under the given parameter set.

S2.2.2 Calibration procedure

Bayes Theorem and the likelihood. We have that $\hat{S}_P \in \Omega \subset \mathbb{R}_{\geq 0}^N$ indicates the set of nondimensional parameter values in the N -dimensional and bounded parameter space Ω , and that $\hat{S}_D = \{\hat{u}_D^i, i = 1, \dots, M\}$ indicates the set of M nondimensional data points \hat{u}_D^i . From Bayes Theorem, the posterior distribution of \hat{S}_P given the data set \hat{S}_D – i.e. the distribution $\mathcal{P}(\hat{S}_P | \hat{S}_D)$ – is such that

$$\mathcal{P}(\hat{S}_P | \hat{S}_D) \propto \mathcal{P}(\hat{S}_P) \mathcal{L}(\hat{S}_P), \quad (\text{S25})$$

where $\mathcal{P}(\hat{S}_P)$ is the prior distribution of \hat{S}_P , and $\mathcal{L}(\hat{S}_P)$ is the likelihood of \hat{S}_P [13]. Assuming Gaussian measurement noise with zero mean [9], the likelihood is given by

$$\mathcal{L}(\hat{S}_P) = \mathbb{P}(\hat{S}_D | \hat{S}_P) = (2\pi\epsilon^2)^{-M/2} \prod_{i=1}^M \exp\left(-\frac{(\hat{u}_D^i - \hat{u}_P^i)^2}{2\epsilon^2}\right), \quad (\text{S26})$$

where $\{\hat{u}_P^i, i = 1, \dots, M\}$ indicates the nondimensional summary statistics predicted by the model under \hat{S}_P .

Likelihood-maximising method. Due to little knowledge on the prior distribution of the parameters, we assume each of them to be uniformly distributed in a bounded domain, and seek \hat{S}_P maximising the likelihood. In practice, we search for the minimum point of the function $-(2\pi\epsilon^2)^{M/2} \mathcal{L}(\hat{S}_P)$, ignoring the normalising factor for convenience as a perfect match with the data would occur at -1 , in the domain assumed for the prior distributions, exploiting the in-built MATLAB function `bayesopt`, which is based on Bayesian Optimisation [12]. Due to little knowledge on the parameter values, we take the assumed domain of the prior distributions of most nondimensional parameters to span several orders of magnitude (details below). These ranges of values are then iteratively updated to ensure that we obtain a good agreement with the experimentally observed MCT1 expression distributions of MCF7-sh-WISP2 cells reported in Fig.2(A) of the Main Manuscript.

Ranges of parameter values considered in the calibration algorithm. We considered the nondimensional parameters to take values in the following ranges: $\hat{\zeta} \in [0, 100]$, $\hat{\gamma}_G, \hat{\gamma}_L, \hat{\alpha}_G, \hat{\alpha}_L, \hat{d}, \hat{\kappa}_G, \hat{\kappa}_L \hat{\eta}_L \in [0, 10]$, $\hat{\lambda}_L, \hat{\lambda}_G \in [0, 1]$ and $\hat{\beta} \in [0, 10^{-1}]$. The Hill coefficients \hat{c} and \hat{m} are assumed to be in the interval $[0.9, 4]$, since most studies assume Michaelis-Menten kinetics (i.e. Hill coefficient equal to 1) but recent works assume positive cooperative binding for glucose uptake [4]. The threshold glucose concentration for lactate uptake is in the interval of experimentally-considered glucose concentrations $\hat{G}^* \in [0, 4.5]$. Finally, for consistency with the mean MCT1 expression levels recorded in the experiments (cf. Fig. 2(B) of the Main Manuscript), we consider $y_L \in [0, 15 \times 10^3]$ and $y_H \in [35 \times 10^3, 100 \times 10^3]$.

S2.3 Optimal parameter sets obtained through model calibration

The optimal parameter sets S_P (up to 4 d.p.) for the mathematical model defined by the PIDE-ODE system (S5), (S18), (S19), subject to the initial conditions defined via Eqs. (S22)-(S24), in which both spontaneous and environment-induced changes in MCT1 expression are included (i.e. the model with $\Phi \not\equiv 0, \Psi^\pm \not\equiv 0$) and for reduced models in which only spontaneous changes in MCT1 expression are included (i.e. the model with $\Phi \not\equiv 0, \Psi^\pm \equiv 0$) or only environment-induced changes in MCT1 expression are included (i.e. the model with $\Phi \equiv 0, \Psi^\pm \not\equiv 0$) are reported in Tab. S1. The value of the normalised likelihood $(2\pi\epsilon^2)^{M/2}\mathcal{L}(S_P)$ related to each parameter set is provided in the last row of Tab. S1, where the likelihood $\mathcal{L}(S_P)$ is defined via Eq. (S26) assuming Gaussian measurement noise with zero mean and variance $\epsilon^2 = 10$ for each of the $M = 21$ data points from *in vitro* experiments. The units of measure of the parameters are reported in the last column, where ‘-’ is reported for dimensionless parameters.

S2.4 Numerical methods for the simulations of the mathematical model

Numerical solutions of the PIDE-ODE system (S5), (S18), (S19) subject to the initial conditions defined via Eqs. (S22)-(S24) are constructed using a uniform discretisation of the interval $[0, T]$, chosen as computational domain of the variable t , with uniform step $\Delta t = 10^{-5}$, and a uniform discretisation of the interval $[-3, 3]$, chosen as computational domain of the variable x , with uniform step $\Delta x = 0.002$. Suitable values of the final time of simulations $T > 0$ are chosen depending on the scenarios under study.

To solve numerically the PIDE (S5), we impose the following zero-flux boundary conditions

$$\begin{cases} \Psi(G(t), L(t)) n_r(t, -3) - \Phi(G(t), L(t), \mu_r(t)) \partial_x n_r(t, -3) = 0, \\ \Psi(G(t), L(t)) n(t, 3) - \Phi(G(t), L(t), \mu_r(t)) \partial_x n_r(t, 3) = 0, \end{cases} \quad \forall t \in (0, T),$$

which are implemented by means of first-order forward (at $x = -3$) and backward (at $x = 3$) finite difference approximations. We make use of first-order forward difference approximation for the time derivative, second-order central difference approximation for the diffusion term, and a first-order upwind scheme to approximate the advection term. Integral terms are approximated by the corresponding left Riemann sums. Given the numerical values of $n_r(t, x)$, $\rho_r(t)$, $\mu_r(t)$ and $\sigma_r^2(t)$, the corresponding values of $n(t, y)$, $\rho(t)$, $\mu(t)$ and $\sigma^2(t)$ are obtained through the change of variable $n(t, y) = (y_H - y_L)^{-1} n_r(t, x)$ and the relations given by Eq. (S4), respectively.

To solve numerically the ODEs (S18) and (S19), we make use of first-order forward difference approximation for the time derivatives, while integral terms are approximated by the corresponding left Riemann sums.

Table S1: Optimal parameter sets obtained through model calibration.

Parameter	Biological meaning	Model with $\Phi \not\equiv 0, \Psi^\pm \not\equiv 0$	Model with $\Phi \equiv 0, \Psi^\pm \not\equiv 0$	Model with $\Phi \not\equiv 0, \Psi^\pm \equiv 0$	Units of measure
y_L	MCT1 level corresponding to the maximum rate of proliferation via glycolysis	3.4843×10^3	2.5284×10^3	9.0602×10^3	-
y_H	MCT1 level corresponding to the maximum rate of proliferation via lactate reuse	67.8279×10^3	68.2576×10^3	70.8045×10^3	-
d	Rate of death due to intracellular competition	0.1238×10^{-6}	0.1213×10^{-6}	0.1181×10^{-6}	/cell /day
γ_G	Maximum rate of proliferation via glycolysis	1.9358	2.0199	1.9536	/day
γ_L	Maximum rate of proliferation via lactate reuse	1.9639	1.9991	1.9328	/day
α_G	Glucose concentration at half receptor occupancy	0.6043	0.5978	0.5314	g/l
α_L	Lactate concentration at half receptor occupancy	6.7510	6.7022	6.7283	mmol/l
m	Hill coefficient for glucose ligand-receptor dynamics	1.0052	0.9931	0.9945	-
c	Hill coefficient for lactate ligand-receptor dynamics	1.0069	1.3526	1.5496	-
G^*	Threshold level of glucose above which lactate uptake stops	1.0079	1.0156	0.9954	g/l
β	Minimum rate of spontaneous changes in MCT1 expression	0.4×10^{-3}	0.35×10^{-2}	/	/day
ζ	Lactate-dependency coefficient of the rate of spontaneous changes in MCT1 expression	5.3190	5.0399	/	-
λ_L	Maximum rate of environment-induced increase in MCT1 expression	0.886×10^{-1}	/	0.1108	/day
λ_G	Maximum rate of environment-induced decrease in MCT1 expression	0.3135	/	0.5552	/day
κ_G	Rate of glucose consumption	0.1786×10^{-6}	0.1723×10^{-6}	0.1692×10^{-6}	g/l /cell /day
κ_L	Rate of lactate production	2.3657×10^{-6}	2.2781×10^{-6}	2.1463×10^{-6}	mmol/l /cell /day
η_L	Conversion factor for lactate consumption	0.23657×10^{-6}	0.2259×10^{-6}	0.2165×10^{-6}	mmol/l /cell
		$(2\pi\epsilon^2)^{M/2}\mathcal{L}(S_P)$ $= 0.9982$	$(2\pi\epsilon^2)^{M/2}\mathcal{L}(S_P)$ $= 0.9981$	$(2\pi\epsilon^2)^{M/2}\mathcal{L}(S_P)$ $= 0.9982$	

S2.5 Analysis of the mathematical model

We first characterise the qualitative and quantitative properties of the solution to the PIDE (S5) subject to the initial condition (S22) (cf. Proposition S2.1) and then study its convergence to equilibrium under fixed concentrations of glucose and lactate (cf. Theorem S2.2).

Proposition S2.1 *Let assumptions (S6) and (S11) hold. Then, the PIDE (S5) subject to the initial condition (S22) admits the exact solution*

$$n_r(t, x) = \frac{\rho_r(t)}{\sqrt{2\pi\sigma_r^2(t)}} \exp\left[-\frac{(x - \mu_r(t))^2}{2\sigma_r^2(t)}\right], \quad (\text{S27})$$

with $\rho_r(t)$, $\mu_r(t)$ and $v_r(t) := 1/\sigma_r^2(t)$ being the components of the solution to the following Cauchy

problem

$$\left\{ \begin{array}{l} \frac{dv_r}{dt} = 2(b(G, L) - \Phi(G, L)v_r^2), \\ \frac{d\mu_r}{dt} = \frac{2b(G, L)}{v_r}(X(G, L) - \mu_r) + \Psi(G, L, \mu_r), \\ \frac{d\rho_r}{dt} = \left[\left(a(G, L) - \frac{b(G, L)}{v_r} - b(G, L)(X(G, L) - \mu_r)^2 \right) - d\rho_r \right] \rho_r, \\ v_r(0) = 1/\sigma_{r0}^2, \quad \mu_r(0) = \mu_{r0}, \quad \rho_r(0) = \rho_{r0}, \end{array} \right. \quad t \in (0, \infty). \quad (\text{S28})$$

Proof. In the remainder of the proof we use the abridged notation

$$a \equiv a(G, L), \quad b \equiv b(G, L), \quad X \equiv X(G, L), \quad \Phi \equiv \Phi(G, L), \quad \Psi \equiv \Psi(G, L, \mu_r)$$

and drop the subscripts r for brevity.

Substituting the definitions given by Eqs.(S6) and (S11) into the PIDE (S5) yields

$$\frac{\partial n}{\partial t} = \Phi \frac{\partial^2 n}{\partial x^2} - \Psi \frac{\partial n}{\partial x} + [a - b(x - X)^2 - d\rho(t)] n, \quad x \in \mathbb{R}. \quad (\text{S29})$$

Building upon the results presented in [1, 5, 11, 16], we make the ansatz (S27). Substituting this ansatz into Eq. (S29) and introducing the notation $v(t) = 1/\sigma^2(t)$ we find

$$\begin{aligned} \frac{1}{\rho} \frac{d\rho}{dt} + \frac{1}{2v} \frac{dv}{dt} &= \frac{1}{2} \frac{dv}{dt} (x - \mu)^2 - \frac{d\mu}{dt} v(x - \mu) + \Phi \left[v^2 (x - \mu)^2 - v \right] + \\ &+ \Psi v(x - \mu) + a - b(x - X)^2 - d\rho. \end{aligned} \quad (\text{S30})$$

Equating the second-order terms in x gives the following differential equation for v

$$\frac{dv}{dt} + 2\Phi v^2 = 2b. \quad (\text{S31})$$

Equating the coefficients of the first-order terms in x , and eliminating $\frac{dv}{dt}$ from the resulting equation, yields

$$\frac{d\mu}{dt} = \frac{2b(X - \mu)}{v} + \Psi. \quad (\text{S32})$$

Choosing $x = \mu$ in Eq. (S30), and eliminating $\frac{dv}{dt}$ from the resulting equation, we obtain

$$\frac{d\rho}{dt} = \left[\left(a - \frac{b}{v} - b(X - \mu)^2 \right) - d\rho \right] \rho. \quad (\text{S33})$$

Under the initial condition given by Eq. (S22), we have

$$v(0) = 1/\sigma_0^2, \quad \mu(0) = \mu_0, \quad \rho(0) = \rho_0,$$

and imposing these initial conditions for the ODEs (S31)-(S33) yields the Cauchy problem (S28). \square

Theorem S2.2 *Let assumptions (S6), (S9), (S11), (S13), (S16) and (S17) hold. Let also*

$$G(t) \equiv \bar{G} \geq 0 \quad \text{and} \quad L(t) \equiv \bar{L} \geq 0. \quad (\text{S34})$$

Then, the solution of the PIDE (S5) subject to the initial condition (S22) is such that

$$\rho_r(t) \longrightarrow \rho_{r\infty}(\bar{G}, \bar{L}), \quad \mu_r(t) \longrightarrow \mu_{r\infty}(\bar{G}, \bar{L}), \quad \sigma_r^2(t) \longrightarrow \sigma_{r\infty}^2(\bar{G}, \bar{L}) \quad \text{as } t \rightarrow \infty, \quad (\text{S35})$$

with

$$\begin{aligned} \rho_{r\infty}(\bar{G}, \bar{L}) &= \max \left(0, \frac{1}{d} \left[a(\bar{G}, \bar{L}) - \sqrt{\Phi(\bar{G}, \bar{L}) b(\bar{G}, \bar{L})} - \frac{(\Psi^+(\bar{G}, \bar{L}))^2}{4\Phi(\bar{G}, \bar{L})} \right] \right), \\ \mu_{r\infty}(\bar{G}, \bar{L}) &= X(\bar{G}, \bar{L}) + \frac{\Psi^+(\bar{G}, \bar{L})}{2\sqrt{\Phi(\bar{G}, \bar{L}) b(\bar{G}, \bar{L})}}, \quad \sigma_{r\infty}^2(\bar{G}, \bar{L}) = \sqrt{\frac{\Phi(\bar{G}, \bar{L})}{b(\bar{G}, \bar{L})}}. \end{aligned} \quad (\text{S36})$$

Proof. Proposition S2.1 ensures that for any $t \in [0, \infty)$ the solution of the PIDE (S5) subject to the initial condition (S22) is of the Gaussian form (S27). Building on the method of proof presented in [2, 5, 16], we thus prove Theorem S2.2 by studying the asymptotic behaviour of the components of the solution to the Cauchy problem (S28) for $t \rightarrow \infty$ under the additional assumption (S34). In the remainder of the proof use the abridged notation

$$a \equiv a(\bar{G}, \bar{L}), \quad b \equiv b(\bar{G}, \bar{L}), \quad X \equiv X(\bar{G}, \bar{L}), \quad \Phi \equiv \Phi(\bar{G}, \bar{L}), \quad \Psi^+ \equiv \Psi^+(\bar{G}, \bar{L}), \quad \Psi^- \equiv \Psi^-(\bar{G}, \mu_r)$$

and drop the subscript r for brevity.

Asymptotic behaviour of $v(t) = 1/\sigma^2(t)$ for $t \rightarrow \infty$. Solving the ODE (S28)₁ subject to the initial condition $v(0) = v_0$ gives

$$v(t) = \sqrt{\frac{b}{\Phi}} \frac{\sqrt{\frac{b}{\Phi}} + v_0 - \left(\sqrt{\frac{b}{\Phi}} - v_0 \right) \exp(-4\sqrt{b\Phi}t)}{\sqrt{\frac{b}{\Phi}} + v_0 + \left(\sqrt{\frac{b}{\Phi}} - v_0 \right) \exp(-4\sqrt{b\Phi}t)}, \quad (\text{S37})$$

which implies that

$$v(t) \longrightarrow \sqrt{\frac{b}{\Phi}} \quad \text{exponentially fast as } t \rightarrow \infty. \quad (\text{S38})$$

Asymptotic behaviour of $\mu(t)$ for $t \rightarrow \infty$. Solving the ODE (S28)₂ subject to the initial condition $\mu(0) = \mu_0$ with the integrating factor method yields

$$\begin{aligned} \mu(t) &= h + (\mu_0 - X) \exp \left[- \int_0^t \left(\frac{2b}{v(z)} + \Psi^- \right) dz \right] + \\ &+ (\Psi^+ - X\Psi^-) \left\{ \int_0^t \exp \left[\int_0^z \left(\frac{2b}{v(\tau)} + \Psi^- \right) d\tau \right] dz \right\} \exp \left[- \int_0^t \left(\frac{2b}{v(z)} + \Psi^- \right) dz \right]. \end{aligned} \quad (\text{S39})$$

We compute the integrals in Eq.(S39) using the solution of the ODE (S28)₁ given by Eq.(S37). Introducing the notation

$$\delta = \frac{\sqrt{b/\Phi} - v_0}{\sqrt{b/\Phi} + v_0}, \quad (\text{S40})$$

we obtain

$$\begin{aligned} \mu(t) &= X + \frac{(1 - \delta)(\mu_0 - X)}{\exp(2\sqrt{b\Phi}t) - \delta \exp(-2\sqrt{b\Phi}t) + (1 - \delta)\Psi^-t} + \\ &+ \frac{(\Psi^+ - X\Psi^-)}{2\sqrt{b\Phi}} \frac{\left[\exp(2\sqrt{b\Phi}t) + \delta \exp(-2\sqrt{b\Phi}t) - (1 + \delta) + (1 - \delta)\Psi^- \sqrt{b\Phi}t^2 \right]}{\left[\exp(2\sqrt{b\Phi}t) - \delta \exp(-2\sqrt{b\Phi}t) + (1 - \delta)\Psi^-t \right]}. \end{aligned}$$

Since, under assumptions (S9), (S13), (S16) and (S17), we have $X \Psi^- \equiv X(\bar{G}, \bar{L}) \Psi^-(\bar{G}, \mu) = 0$ for any $\bar{G} \geq 0$, the latter expression of $\mu(t)$ allows us to conclude that

$$\mu(t) \longrightarrow X + \frac{\Psi^+}{2\sqrt{b\Phi}} \quad \text{exponentially fast as } t \rightarrow \infty. \quad (\text{S41})$$

Asymptotic behaviour of $\rho(t)$ for $t \rightarrow \infty$. We define

$$w \equiv w(t) \equiv w(v(t), \mu(t), \bar{G}, \bar{L}) = \left(\sqrt{b\Phi} - \frac{b}{v} \right) - b \left(\mu - X - \frac{\Psi^+}{2\sqrt{b\Phi}} \right)^2$$

and rewrite the ODE (S28)₃ as

$$\frac{d\rho}{dt} = \left[\left(a + \frac{(\Psi^+)^2}{4\Phi} - \sqrt{b\Phi} - \Psi^+ \sqrt{\frac{b}{\Phi}} (\mu - X) + w \right) - d\rho \right] \rho. \quad (\text{S42})$$

Solving Eq.(S42) subject to the initial condition $\rho(0) = \rho_0$ yields

$$\rho(t) = \frac{\rho_0 \exp \left[\left(a + \frac{(\Psi^+)^2}{4\Phi} - \sqrt{b\Phi} \right) t - \Psi^+ \sqrt{\frac{b}{\Phi}} \int_0^t (\mu(z) - X) dz + \int_0^t w(z) dz \right]}{1 + d \rho_0 \int_0^t \exp \left[\left(a + \frac{(\Psi^+)^2}{4\Phi} - \sqrt{b\Phi} \right) z - \Psi^+ \sqrt{\frac{b}{\Phi}} \int_0^z (\mu(\tau) - X) d\tau + \int_0^z w(\tau) d\tau \right] dz}. \quad (\text{S43})$$

The asymptotic results (S38) and (S41) ensure that

$$w(t) \longrightarrow 0 \quad \text{exponentially fast as } t \rightarrow \infty. \quad (\text{S44})$$

Furthermore, the asymptotic results (S41) and (S44) imply that in the asymptotic regime $t \rightarrow \infty$ we have

$$\begin{aligned} & \exp \left[\left(a + \frac{(\Psi^+)^2}{4\Phi} - \sqrt{b\Phi} \right) t - \Psi^+ \sqrt{\frac{b}{\Phi}} \int_0^t (\mu(z) - X) dz + \int_0^t w(z) dz \right] \\ & \sim A \exp \left[\left(a - \sqrt{b\Phi} - \frac{(\Psi^+)^2}{4\Phi} \right) t \right], \end{aligned} \quad (\text{S45})$$

for some positive constant factor $A \equiv A(\bar{G}, \bar{L})$. Therefore, Eq. (S43) allows us to conclude that

$$\text{if } \sqrt{b\Phi} + \frac{(\Psi^+)^2}{4\Phi} \geq a \quad \text{then} \quad \rho(t) \longrightarrow 0 \quad \text{as } t \rightarrow \infty. \quad (\text{S46})$$

On the other hand, the asymptotic results (S41) and (S44) imply that, if $\sqrt{b\Phi} + (\Psi^+)^2/(4\Phi) < a$, in the asymptotic regime $t \rightarrow \infty$ we also have

$$\begin{aligned} & \int_0^t \exp \left[\left(a + \frac{(\Psi^+)^2}{4\Phi} - \sqrt{b\Phi} \right) z - \Psi^+ \sqrt{\frac{b}{\Phi}} \int_0^z (\mu(\tau) - X) d\tau + \int_0^z w(\tau) d\tau \right] dz \\ & \sim B \frac{\exp \left[\left(a - \sqrt{b\Phi} - \frac{(\Psi^+)^2}{4\Phi} \right) t \right]}{\left(a - \sqrt{b\Phi} - \frac{(\Psi^+)^2}{4\Phi} \right)}, \end{aligned} \quad (\text{S47})$$

for some positive constant factor $B \equiv B(\bar{G}, \bar{L})$. The asymptotic relations (S45) and (S47), along with Eq. (S43), allow us to conclude that

$$\text{if } \sqrt{b\Phi} + \frac{(\Psi^+)^2}{4\Phi} < a \quad \text{then} \quad \rho(t) \longrightarrow \frac{1}{d} \left[a - \sqrt{b\Phi} - \frac{(\Psi^+)^2}{4\Phi} \right] \quad \text{as } t \rightarrow \infty. \quad (\text{S48})$$

Taken together, the asymptotic results (S46) and (S48) yield

$$\rho(t) \longrightarrow \max \left(0, \frac{1}{d} \left[a - \sqrt{b\Phi} - \frac{(\Psi^+)^2}{4\Phi} \right] \right) \quad \text{as } t \rightarrow \infty. \quad (\text{S49})$$

Claims (S35) and (S36) follow from the asymptotic results (S38), (S41) and (S49).

Remark S2.3 *The asymptotic results of Theorem S2.2 along with the relations given by Eq. (S4) imply that, when $(G(t), L(t)) \equiv (\bar{G}, \bar{L})$,*

$$\rho(t) \longrightarrow \rho_\infty(\bar{G}, \bar{L}), \quad \mu(t) \longrightarrow \mu_\infty(\bar{G}, \bar{L}), \quad \sigma^2(t) \longrightarrow \sigma_\infty^2(\bar{G}, \bar{L}) \quad \text{as } t \rightarrow \infty, \quad (\text{S50})$$

where

$$\begin{aligned} \rho_\infty(\bar{G}, \bar{L}) &= \max \left(0, \frac{1}{d} \left[a(\bar{G}, \bar{L}) - \sqrt{\Phi(\bar{G}, \bar{L}) b(\bar{G}, \bar{L})} - \frac{(\Psi^+(\bar{G}, \bar{L}))^2}{4\Phi(\bar{G}, \bar{L})} \right] \right), \\ \mu_\infty(\bar{G}, \bar{L}) &= y_L + (y_H - y_L) \left[X(\bar{G}, \bar{L}) + \frac{\Psi^+(\bar{G}, \bar{L})}{2\sqrt{\Phi(\bar{G}, \bar{L}) b(\bar{G}, \bar{L})}} \right], \\ \sigma_\infty^2(\bar{G}, \bar{L}) &= (y_H - y_L)^2 \sqrt{\frac{\Phi(\bar{G}, \bar{L})}{b(\bar{G}, \bar{L})}}. \end{aligned} \quad (\text{S51})$$

S3 Supplementary figures

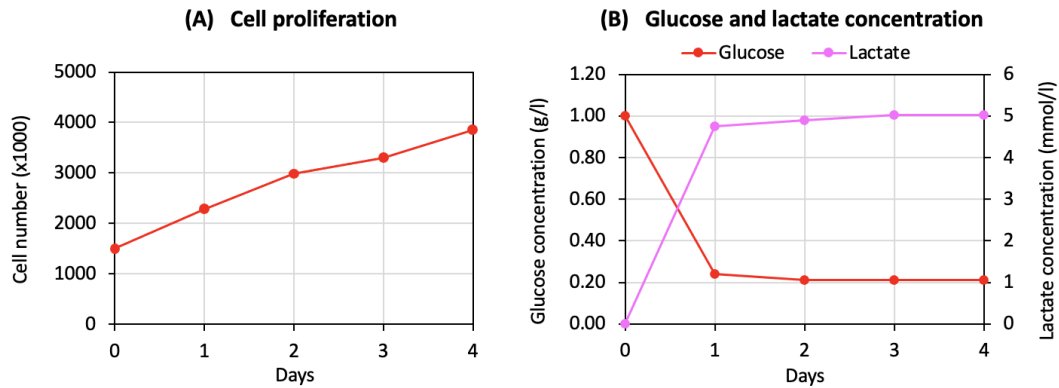


Figure S1: **Dynamics of cell proliferation and glucose and lactate concentrations in ‘glucose-deprivation’ experiments conducted on MCF7 cells.** Dynamics of cell proliferation (panel (A)), glucose concentration (panel (B), red line, left y-axis) and lactate concentration (panel (B), pink line, right y-axis) in ‘glucose-deprivation’ experiments conducted on MCF7 cells for four days. Cell proliferation was assessed by counting the number of viable cells upon seeding (i.e. day 0) and at the end of each day of culture (i.e. days 1-4). Glucose and lactate concentrations were measured in the culture medium at days 0-4.

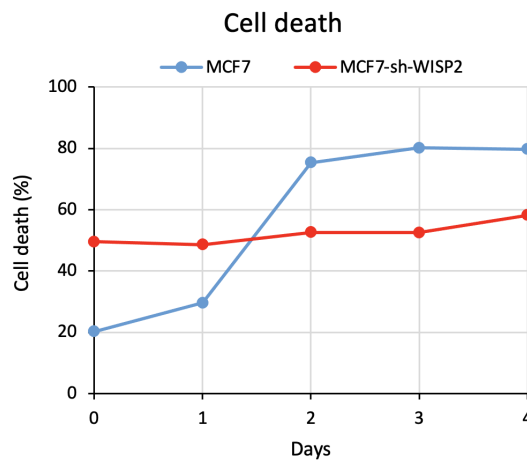


Figure S2: **Dynamics of cell death in ‘glucose-deprivation’ experiments conducted on MCF7 and MCF7-sh-WISP2 cells.** Dynamics of cell death in ‘glucose-deprivation’ experiments conducted on MCF7 cells (blue line) and MCF7-sh-WISP2 cells (red line) for four days. Cell death was assessed by measuring the percentage of apoptotic cells upon seeding (i.e. day 0) and at the end of each day of culture (i.e. days 1-4).

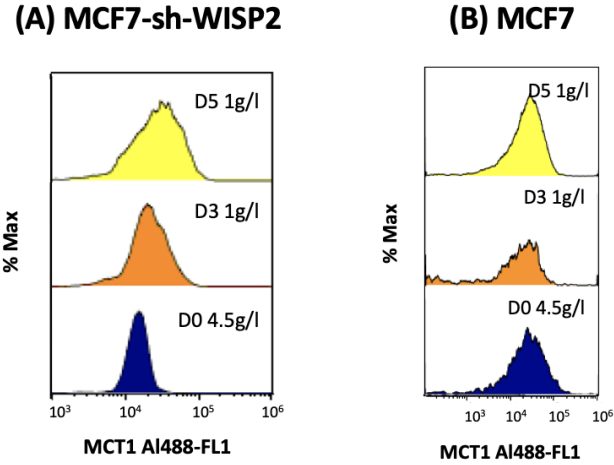


Figure S3: **Dynamics of MCT1 expression in ‘glucose-deprivation’ experiments conducted on MCF7-sh-WISP2 and MCF7 cells.** Comparison between MCT1 protein expression of MCF7-sh-WISP2 cells (panel (A)) and MCF7 cells (panel (B)), assessed through flow cytometry analysis, upon seeding (i.e. on day 0) and on days 3 and 5 of ‘glucose-deprivation’ experiments conducted for five days (sub-panel D0 and sub-panels D3 and D5).

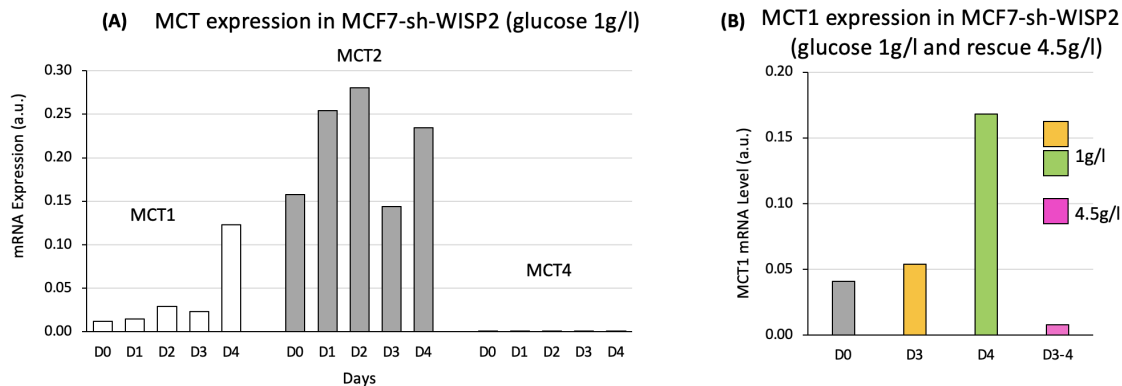


Figure S4: **Dynamics of MCT expression in ‘glucose-deprivation’ and ‘rescue’ experiments conducted on MCF7-sh-WISP2 cells.** (A) MCT1, MCT2 and MCT4 mRNA expression of MCF7-sh-WISP2 cells, assessed through RT-qPCR, upon seeding (i.e. on day 0) and on days 1-4 of ‘glucose-deprivation’ experiments conducted for four days (column D0 and columns D1-D4). (B) MCT1 mRNA expression of MCF7-sh-WISP2 cells, assessed through RT-qPCR, upon seeding (i.e. on day 0) and on days 3 and 4 of ‘glucose-deprivation’ experiments conducted for four days (column D0 and columns D3 and D4). MCT1 mRNA expression during the phase of rescue from glucose deprivation in the corresponding ‘rescue’ experiments (i.e. on days 3 and 4) is also displayed (column D3-4). The mRNA levels in the plots indicate the abundance of the target gene relative to that of endogenous control Actin used to normalise the initial quantity and purity of total RNA.

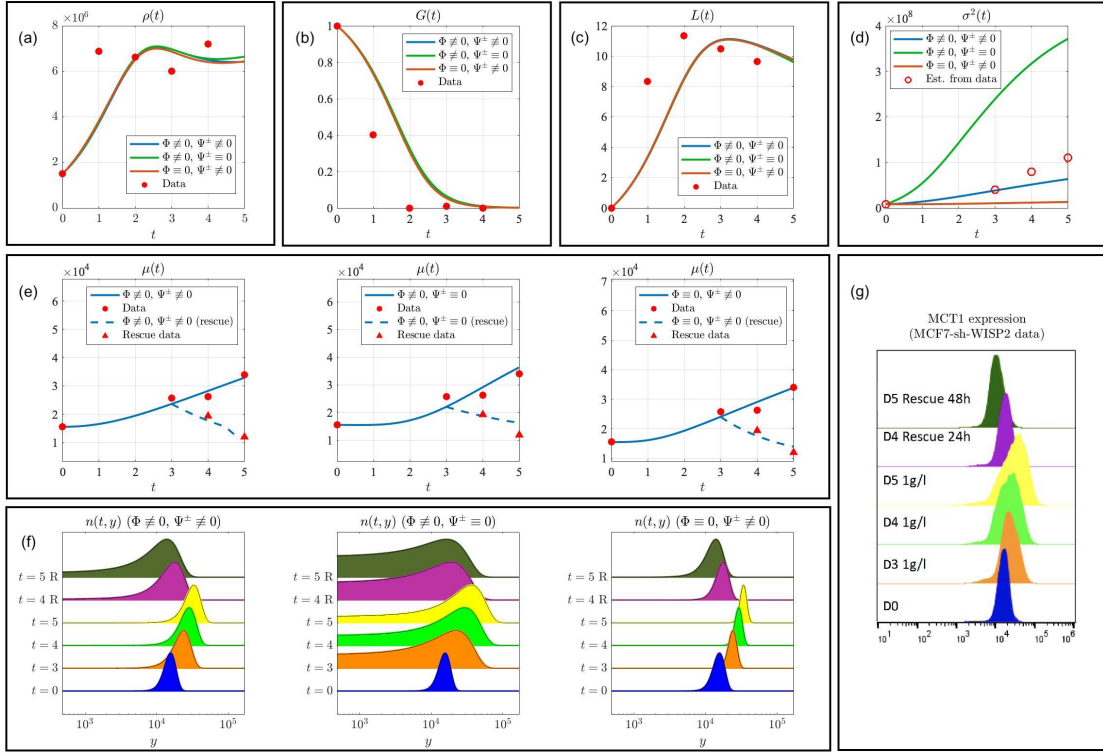


Figure S5: Numerical simulations of ‘glucose-deprivation’ and ‘rescue’ experiments conducted on MCF7-sh-WISP2 cells. Simulated dynamics of the cell number $\rho(t)$ (panel (a)), the glucose concentration $G(t)$ (panel (b)), the lactate concentration $L(t)$ (panel (c)), the mean level of MCT1 expression $\mu(t)$ (solid lines, panel (e)), the related variance $\sigma^2(t)$ (panel (d)), and the MCT1 expression distribution $n(t, y)$ (panel (f), $t = 0 - t = 5$) in ‘glucose-deprivation’ experiments conducted on MCF7-sh-WISP2 cells. Numerical simulations were carried out for the calibrated model in which both spontaneous and environment-induced changes in MCT1 expression are included (i.e. $\Phi \not\equiv 0, \Psi^\pm \not\equiv 0$) and for calibrated reduced models in which only spontaneous changes in MCT1 expression are included (i.e. $\Phi \not\equiv 0, \Psi^\pm \equiv 0$) or only environment-induced changes in MCT1 expression are included (i.e. $\Phi \equiv 0, \Psi^\pm \not\equiv 0$), under the OPS reported in Tab.S1. The MCT1 expression distribution is plotted on the logarithmic scale as for the outputs of flow cytometry analyses (panel (g)) to facilitate visual comparison. MCT1 expression distributions during the phase of rescue from glucose deprivation in the corresponding simulations of ‘rescue’ experiments are also displayed (panel (f), $t = 4$ R and $t = 5$ R) along with the mean levels of MCT1 expression (panel (e), dashed lines). The red markers highlight experimental data that are used to carry out model calibration, with circles and triangles corresponding to ‘glucose-deprivation’ and ‘rescue’ experiments, respectively. The values of t are in days, the values of $G(t)$ are in g/l, and the values of $L(t)$ are in mmol/l.

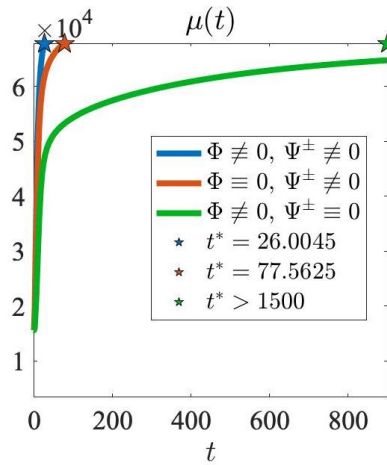


Figure S6: Numerical simulations of long-term dynamics of the mean level of MCT1 expression of glucose-deprived MCF7-sh-WISP2 cells. Long-term dynamics of the mean level of MCT1 expression of MCF7-sh-WISP2 cells $\mu(t)$ in ‘glucose-deprivation’ experiments simulated through the calibrated model in which both spontaneous and environment-induced changes in MCT1 expression are included (i.e. $\Phi \neq 0, \Psi^\pm \neq 0$) and through calibrated reduced models in which only environment-induced changes in MCT1 expression are included (i.e. $\Phi \equiv 0, \Psi^\pm \neq 0$) or only spontaneous changes in MCT1 expression are included (i.e. $\Phi \neq 0, \Psi^\pm \equiv 0$), under the OPS reported in Tab.S1. Dynamics are shown for $t \in [0, t^*]$ (in days), with t^* being the first time instant when the mean level of MCT1 expression attains the value y_H , which in our modelling framework is the level endowing MCF7-sh-WISP2 cells with the maximum capability of taking lactate from the extracellular environment and reusing it to produce the energy required for their proliferation under glucose deprivation. The value of t^* is marked by a star, i.e. $t^* = 26.0045$ for the model with $\Phi \neq 0$ and $\Psi^\pm \neq 0$, $t^* = 77.5625$ for the model with $\Phi \equiv 0$ and $\Psi^\pm \neq 0$, and $t^* > 1500$ for the model with $\Phi \neq 0$ and $\Psi^\pm \equiv 0$.

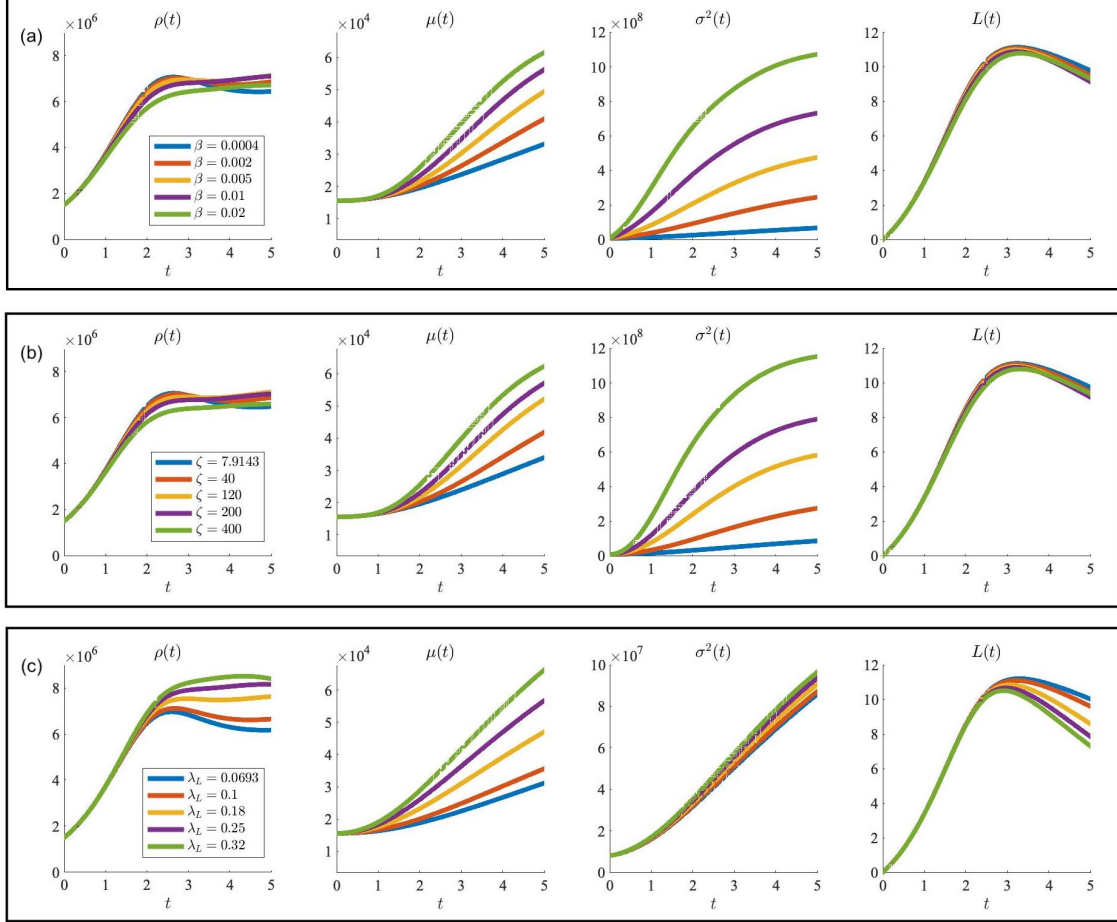


Figure S7: Additional numerical simulations of ‘glucose-deprivation’ experiments conducted on MCF7-sh-WISP2 cells. Simulated dynamics of the cell number $\rho(t)$ (first column), the mean level of MCT1 expression $\mu(t)$ (second column), the related variance $\sigma^2(t)$ (third column), and the lactate concentration $L(t)$ (fourth column) in ‘glucose-deprivation’ experiments conducted on MCF7-sh-WISP2 cells. Numerical simulations were carried out for the calibrated model in which both spontaneous and environment-induced changes in MCT1 expression are included (i.e. $\Phi \not\equiv 0$, $\Psi^\pm \not\equiv 0$), under the OPS reported in Tab.S1 but for different values of the parameter β (panel (a)) or different values of the parameter ζ (panel (b)), which correspond to different values of the rate of spontaneous changes in MCT1 expression Φ (cf. the definition given by Eq.(S15)), or different values of the parameter λ_L (panel (c)), which correspond to different values of the rate at which environment-induced changes lead to an increase in MCT1 expression Ψ^+ (cf. the definition given by Eq.(S17)). In particular: in panel (a), $\beta = 0.0004$ (blue lines), $\beta = 0.002$ (orange lines), $\beta = 0.005$ (yellow lines), $\beta = 0.01$ (purple lines), and $\beta = 0.02$ (green lines); in panel (b), $\zeta = 7.9143$ (blue lines), $\zeta = 40$ (orange lines), $\zeta = 120$ (yellow lines), $\zeta = 200$ (purple lines), and $\zeta = 400$ (green lines); in panel (c), $\lambda_L = 0.0693$ (blue lines), $\lambda_L = 0.1$ (orange lines), $\lambda_L = 0.18$ (yellow lines), $\lambda_L = 0.25$ (purple lines), and $\lambda_L = 0.32$ (green lines).

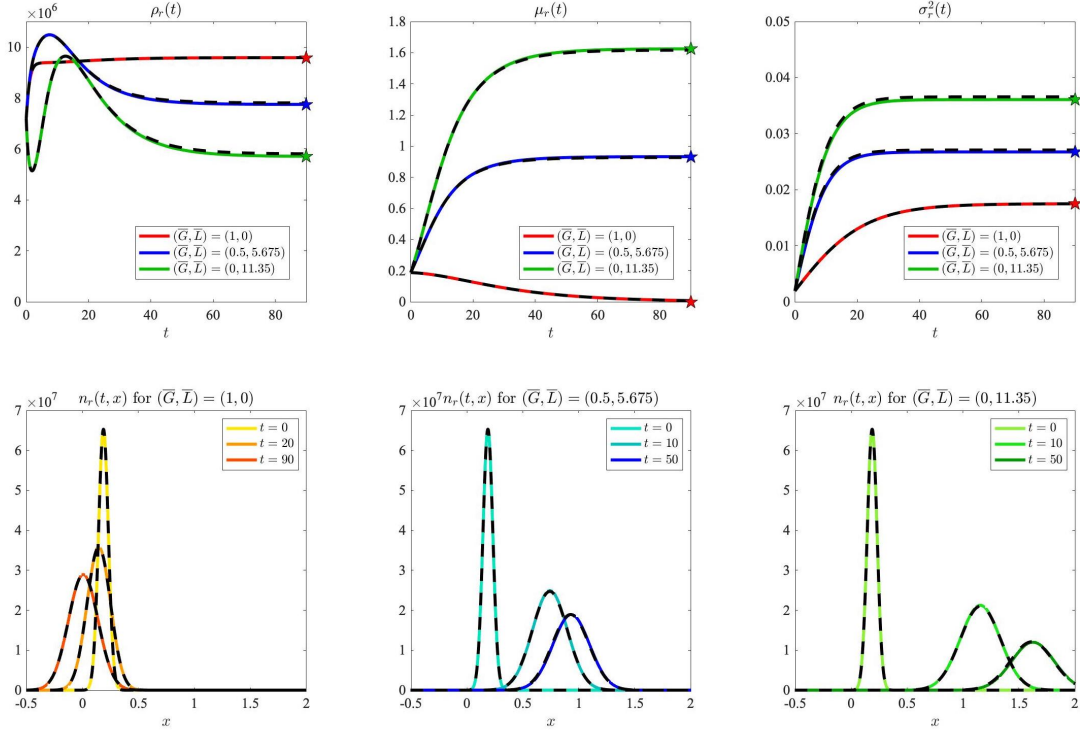


Figure S8: Numerical simulations of long-term dynamics of glucose-deprived MCF7-sh-WISP2 cells under constant concentrations of glucose and lactate. Top row. Simulated dynamics of the cell number $\rho_r(t)$ (first column), the rescaled mean level of MCT1 expression $\mu_r(t)$ (second column), and the related variance $\sigma_r^2(t)$ (third column) under constant concentrations of glucose and lactate, i.e. $(G(t), L(t)) \equiv (\bar{G}, \bar{L})$ with $(\bar{G}, \bar{L}) = (1, 0)$ (red lines), $(\bar{G}, \bar{L}) = (0.5, 5.675)$ (blue lines) and $(\bar{G}, \bar{L}) = (0, 11.35)$ (green lines). Numerical simulations were carried out for the calibrated model in which both spontaneous and environment-induced changes in MCT1 expression are included (i.e. $\Phi \neq 0$, $\Psi^\pm \neq 0$), under the OPS for cell dynamics reported in Tab.S1. The black, dashed lines highlight the dynamics of the same quantities obtained by solving numerically the Cauchy problem (S28) complemented with Eq. (S23) and with $(G(t), L(t)) \equiv (\bar{G}, \bar{L})$, while the coloured stars mark the analytical equilibrium values computed via Eq.(S36). **Bottom row.** Corresponding dynamics of the rescaled MCT1 expression distribution $n_r(t, x)$ for $(\bar{G}, \bar{L}) = (1, 0)$ (left panel), $(\bar{G}, \bar{L}) = (0.5, 5.675)$ (central panel) and $(\bar{G}, \bar{L}) = (0, 11.35)$ (right panel). Coloured, solid lines refer to different times t and the black, dashed lines highlight the rescaled MCT1 expression distribution given by Eq. (S27) whereby $\rho_r(t)$, $\mu_r(t)$ and $\sigma_r^2(t)$ are obtained by solving numerically the Cauchy problem (S28) complemented with Eq. (S23) and with $(G(t), L(t)) \equiv (\bar{G}, \bar{L})$.

References

- [1] L. ALMEIDA, P. BAGNERINI, G. FABRINI, B. D. HUGHES, AND T. LORENZI, *Evolution of cancer cell populations under cytotoxic therapy and treatment optimisation: insight from a phenotype-structured model*, ESAIM: Mathematical Modelling and Numerical Analysis, 53 (2019), pp. 1157–1190.
- [2] A. ARDAŠEVA, R. A. GATENBY, A. R. ANDERSON, H. M. BYRNE, P. K. MAINI, AND T. LORENZI, *Evolutionary dynamics of competing phenotype-structured populations in periodically fluctuating environments*, Journal of Mathematical Biology, 80 (2020), pp. 775–807.
- [3] G. BERGERS AND S.-M. FENDT, *The metabolism of cancer cells during metastasis*, Nature Reviews Cancer, 21 (2021), pp. 162–180.
- [4] G. L. CELORA, H. M. BYRNE, C. E. ZOIS, AND P. G. KEVREKIDIS, *Phenotypic variation modulates the growth dynamics and response to radiotherapy of solid tumours under normoxia and hypoxia*, Journal of Theoretical Biology, 527 (2021), p. 110792.
- [5] R. H. CHISHOLM, T. LORENZI, L. DESVILLETTES, AND B. D. HUGHES, *Evolutionary dynamics of phenotype-structured populations: from individual-level mechanisms to population-level consequences*, Zeitschrift für angewandte Mathematik und Physik, 67 (2016), pp. 1–34.
- [6] R. H. CHISHOLM, T. LORENZI, A. LORZ, A. K. LARSEN, L. ALMEIDA, A. ESCARGUEIL, AND J. CLAIRAMBAULT, *Emergence of drug tolerance in cancer cell populations: an evolutionary outcome of selection, non-genetic instability and stress-induced adaptation*, Cancer Research, 75 (2015), pp. 930–939.
- [7] N. FERRAND, A. GNANAPRAGASAM, G. DOROTHEE, G. REDEUILH, A. K. LARSEN, AND M. SABBAH, *Loss of WISP2/CCN5 in estrogen-dependent MCF7 human breast cancer cells promotes a stem-like cell phenotype*, PloS One, 9 (2014), p. e87878.
- [8] A. FRITAH, C. SAUCIER, O. DE WEVER, M. BRACKE, I. BIÈCHE, R. LIDEREAU, C. GESPACH, S. DROUOT, G. REDEUILH, AND M. SABBAH, *Role of WISP-2/CCN5 in the maintenance of a differentiated and noninvasive phenotype in human breast cancer cells*, Molecular and Cellular Biology, 28 (2008), pp. 1114–1123.
- [9] N. J. LINDEN, B. KRAMER, AND P. RANGAMANI, *Bayesian parameter estimation for dynamical models in systems biology*, bioRxiv, (2022).
- [10] T. LORENZI, R. H. CHISHOLM, AND J. CLAIRAMBAULT, *Tracking the evolution of cancer cell populations through the mathematical lens of phenotype-structured equations*, Biology Direct, 11 (2016), p. 43.
- [11] T. LORENZI, R. H. CHISHOLM, L. DESVILLETTES, AND B. D. HUGHES, *Dissecting the dynamics of epigenetic changes in phenotype-structured populations exposed to fluctuating environments*, Journal of Theoretical Biology, 386 (2015), pp. 166–176.
- [12] R. MARTINEZ-CANTIN, *BayesOpt: a Bayesian optimization library for nonlinear optimization, experimental design and bandits*, Journal of Machine Learning Research, 15 (2014), pp. 3735–3739.
- [13] I. J. MYUNG, *Tutorial on maximum likelihood estimation*, Journal of Mathematical Psychology, 47 (2003), pp. 90–100.
- [14] M. SANTILLÁN, *On the use of the Hill functions in mathematical models of gene regulatory networks*, Mathematical Modelling of Natural Phenomena, 3 (2008), pp. 85–97.

- [15] P. VAUPEL, F. KALLINOWSKI, AND P. OKUNIEFF, *Blood flow, oxygen and nutrient supply, and metabolic microenvironment of human tumors: a review*, Cancer Research, 49 (1989), pp. 6449–6465.
- [16] C. VILLA, M. A. CHAPLAIN, AND T. LORENZI, *Evolutionary dynamics in vascularised tumours under chemotherapy: Mathematical modelling, asymptotic analysis and numerical simulations*, Vietnam Journal of Mathematics, 49 (2021), pp. 143–167.
- [17] D. ZHANG, Z. TANG, H. HUANG, G. ZHOU, C. CUI, Y. WENG, W. LIU, S. KIM, S. LEE, M. PEREZ-NEUT, ET AL., *Metabolic regulation of gene expression by histone lactylation*, Nature, 574 (2019), pp. 575–580.